J. Fluid Mech. (2003), *vol.* 496, *pp.* 213–242. © 2003 Cambridge University Press
DOI: 10.1017/S0022112003006347 Printed in the United Kingdom

Three-dimensional instability of standing waves

By QIANG ZHU, YUMING LIU AND DICK K. P. YUE†

Department of Ocean Engineering, Massachusetts Institute of Technology, Cambridge, MA 02139, USA

(Received 18 September 2002 and in revised form 26 June 2003)

We investigate the three-dimensional instability of finite-amplitude standing surface waves under the influence of gravity. The analysis employs the transition matrix (TM) approach and uses a new high-order spectral element (HOSE) method for computation of the nonlinear wave dynamics. HOSE is an extension of the original high-order spectral method (HOS) wherein nonlinear wave–wave and wave–body interactions are retained up to high order in wave steepness. Instead of global basis functions in HOS, however, HOSE employs spectral elements to allow for complex free-surface geometries and surface-piercing bodies. Exponential convergence of HOS with respect to the total number of spectral modes (for a fixed number of elements) and interaction order is retained in HOSE. In this study, we use TM-HOSE to obtain the stability of general three-dimensional perturbations (on a two-dimensional surface) on two classes of standing waves: plane standing waves in a rectangular tank; and radial/azimuthal standing waves in a circular basin. For plane standing waves, we confirm the known result of two-dimensional side-bandlike instability. In addition, we find a novel three-dimensional instability for base flow of any amplitude. The dominant component of the unstable disturbance is an oblique (standing) wave oriented at an arbitrary angle whose frequency is close to the (nonlinear) frequency of the original standing wave. This finding is confirmed by direct long-time simulations using HOSE which show that the nonlinear evolution leads to classical Fermi–Pasta–Ulam recurrence. For the circular basin, we find that, beyond a threshold wave steepness, a standing wave (of nonlinear frequency Ω) is unstable to three-dimensional perturbations. The unstable perturbation contains two dominant (standing-wave) components, the sum of whose frequencies is close to 2Ω. From the cases we consider, the critical wave steepness is found to generally decrease/increase with increasing radial/azimuthal mode number of the base standing wave. Finally, we show that the instability we find for both two- and three-dimensional standing waves is a result of third-order (quartet) resonance.

1. Introduction

The instability of surface gravity waves is a fundamental problem in nonlinear wave dynamics. The understanding of wave instability is of essential interest to the prediction of steep/breaking wave development and nonlinear wave-field evolution. For propagating waves, the stability has been relatively well studied (see Yuen & Lake 1980 for a review). Benjamin & Feir (1967) showed that a Stokes wave of small steepness is unstable to a sideband disturbance. Longuet–Higgins (1978*a*, *b*) generalized their analysis to finite-amplitude Stokes waves with the inclusion of

† Author to whom correspondence should be addressed.

https://doi.org/10.1017/S0022112003006347 Published online by Cambridge University Press

superharmonic and subharmonic disturbances. When three-dimensional disturbances are taken into account, McLean (1982) found the Class I and Class II instabilities, respectively resulting from the third-order quartet and fourth-order quintet wave resonances between the Stokes wave and the disturbances. Among other implications, nonlinear evolution of a Stokes wave with such three-dimensional disturbances can lead to the development of three-dimensional crescent waves observed in the field/tank (Su 1982; Xue *et al.* 2001).

Instability of standing waves is a more challenging subject because of the unsteadiness of the base flow. The associated linear analysis is more involved both in the determination of the (nonlinear) base flow and in the need to consider an unsteady evolution problem. Existing work typically requires the evaluation of a transition matrix (numerically) on which an eigenvalue analysis is then performed. Results are limited and are available for the two-dimensional problem only. Mercer & Roberts (1992, hereinafter referred to as MR) examined the instability of a plane standing wave to two-dimensional disturbances using fully nonlinear numerical simulations. It is found that, like Stokes waves, plane standing waves are unstable to sideband disturbances. A similar result may also be inferred from the instability of a pair of counter-propagating plane waves (Ioualalen & Kharif 1994; Ioualalen, Roberts & Kharif 1996; Kimmoun, Ioualalen & Kharif 1999). Pierce & Knobloch (1994) investigated the instability of plane standing waves (including surface tension) subject to long transverse modulations. Instability of plane standing waves to general three-dimensional (in two horizontal dimensions) disturbances has not been investigated.

For the stability of three-dimensional standing waves, the quantitative determination of the nonlinear base standing wave is itself a challenge. For axisymmetric standing waves in a circular basin, for example, Mack (1962) derived a perturbation solution up to third order in the wave steepness. Using the collocation method of Vanden-Broeck & Schwartz (1981), Tsai & Yue (1987) developed a numerical method for the fully nonlinear problem, still only for the axisymmetric case. For standing waves in a rectangular basin, Bridges (1987) found the existence of cnoidal standing waves at the critical width/length ratio of the basin, resulting from secondary bifurcation.

No direct computational work exists for the instability of three-dimensional standing waves although a number of experimental investigations reveal interesting energy transfer mechanisms among standing wave modes. In an experimental study of wave motions inside a vertically oscillating circular tank, Gollub & Meyer (1983) discovered that the standing waves in the tank may switch from axisymmetric to non-axisymmetric patterns as the oscillation amplitude increases. A similar symmetry-breaking phenomenon was also observed with propagating surface waves generated by an oscillating half-submerged sphere in an open domain (Martin 1932; Becker & Miles 1992). Based on an average Lagrangian method, Miles (1984*a–c*) carried out a series of theoretical studies of the internal resonant interaction of standing waves in a circular tank, which occurs at the second order in wave steepness.

In this work, we consider the two- and three-dimensional instability of finite-amplitude standing waves in a rectangular and a circular basin. For the stability analysis, we apply the transition matrix method for unsteady flows (e.g. von Kerczek & Davis 1975). The method requires not only the precise determination of the nonlinear base flow but also the calculation of the transition matrix to high accuracy. To accomplish this, we develop a new high-order spectral element (HOSE) method which is an extension of the high-order spectral (HOS) method for nonlinear wave interactions (Dommermuth & Yue 1987). Since its introduction, HOS has been extended to problems involving submerged bodies (e.g. Liu, Dommermuth & Yue

https://doi.org/10.1017/S0022112003006347 Published online by Cambridge University Press

1992) and variable bottom topography (e.g. Liu & Yue 1998). The use of the global basis function in HOS makes problems involving complex free-surface domains impossible and surface piercing body boundaries heretofore unattainable.

HOSE overcomes these limitations by using spectral elements. Like HOS, HOSE accounts for nonlinear wave interactions up to a high order (M) in wave steepness. Within each element, local spectral expansions are used while the solutions at the element and domain boundaries are matched to assure the necessary smoothness. The exponential convergence of HOS with respect to both M and the (total) number of spectral modes N (for a fixed number of elements) is retained in HOSE. Significantly, HOSE robustly solves problems involving complex free-surface domains and surface-piercing bodies. In the present context, the accuracy and efficacy of HOSE allow a direct computational analysis of the stability of nonlinear two- and three-dimensional standing waves in tanks.

We first revisit the two-dimensional problem where the instability of plane standing waves to two-dimensional disturbances (i.e. one-dimensional surface) is considered. For this relatively simple case, we confirm MR's finding of side-bandlike instability and obtain quantitative comparisons with MR's results on the frequency and growth rate of unstable disturbances. For the new case of the three-dimensional stability of plane standing waves, we found an instability for all amplitudes of the base standing wave. The dominant component of the unstable mode is an oblique standing wave whose frequency is close to that of the base standing wave. Such an oblique wave component can exist at an arbitrary angle to the base standing wave (although the growth rate varies). We perform long-time direct simulations to confirm such three-dimensional instabilities and find that the nonlinear evolution results in classical Fermi–Pasta–Ulam recurrence (see figure 9 for an example of the free-surface wave-pattern change in the evolution cycle).

For three-dimensional standing waves in a circular basin, we find that when the wave steepness exceeds a threshold value, they are unstable to small three-dimensional perturbations. The unstable perturbation consists of two dominant standing-wave components with (linear) frequencies ω_1 and ω_2 which satisfy $\omega_1 + \omega_2 \simeq 2\Omega$, where Ω is the nonlinear frequency of the nonlinear base standing wave. (Hereinafter, we use uppercase Ω to denote the nonlinear standing-wave frequency which is a function of wave steepness; and lowercase ω to denote linear standing-wave frequencies satisfying the linear dispersion relation.) For a non-axisymmetric standing wave with wavenumber $k_{\ell,\nu}$ ($\ell \geqslant 0$), where ℓ and ν are, respectively, the mode number in the azimuthal and radial directions, the unstable mode has dominant standing-wave components with wavenumbers $\kappa_{\ell-1,\nu+1}$ and $\kappa_{\ell+1,\nu-1}$ (or $\kappa_{\ell-1,\nu}$ and $\kappa_{\ell+1,\nu}$). For an axisymmetric base flow, $\ell = 0$, the unstable wave has dominant components $\kappa_{1,\nu-1}$ and $\kappa_{1,\nu}$. The critical wave steepness of the base standing wave above which such instabilities obtain is found to decrease (increase) with ν (ℓ). (See figure 15 for examples of the three-dimensional free-surface patterns resulting from such instabilities.)

Finally, we perform a frequency component analysis of the nonlinear wave interaction mechanisms and show that the two- and three-dimensional instabilities we find are associated with nonlinear (third-order quartet and higher) resonant interactions between the base flow and the unstable mode. The mechanism of such nonlinear resonance of standing waves resembles the internal combination resonance observed, for example, in beams and plates (e.g. Nayfeh & Mook 1979).

The rest of the paper is organized as follows. In § 2, the transition matrix method for the stability analysis of unsteady flow is reviewed for completeness. The detailed formulation for HOSE as well as systematic verification and convergence tests

https://doi.org/10.1017/S0022112003006347 Published online by Cambridge University Press

for HOSE are presented in § 3. In § 4, computational results for the instability of rectangular and circular base standing waves are presented. The mechanism of instability for standing waves is discussed in § 5. In § 6, conclusions are drawn.

2. The transition matrix method for instability of standing waves

We first present the initial boundary-value problem for the (standing) wave motion in a tank (or basin), in the context of potential flow. We define a Cartesian coordinate system $\boldsymbol{r} \equiv (x, y, z)$ with the vertical axis z positive upwards and $z = 0$ on the mean free surface. For later convenience, we also define a polar coordinate system (r, θ) in the horizontal plane with $x = r\cos\theta$ and $y = r\sin\theta$. Inside the fluid, the velocity potential $\Phi(\boldsymbol{r}, t)$ satisfies the Laplace equation:

$$\Phi_{xx} + \Phi_{yy} + \Phi_{zz} = 0. \tag{2.1}$$

On the instantaneous free surface, $z = \zeta(\boldsymbol{x}, t)$ where $\boldsymbol{x} \equiv (x, y)$, the nonlinear kinematic and dynamic boundary conditions are written in Zakharov's form (Zakharov 1968):

$$\left.\begin{aligned} &\zeta_t + \nabla_{\boldsymbol{x}}\zeta \cdot \nabla_{\boldsymbol{x}}\Phi^s - (1 + \nabla_{\boldsymbol{x}}\zeta \cdot \nabla_{\boldsymbol{x}}\zeta)\Phi^s_z = 0, \\ &\Phi^s_t + g\zeta + \tfrac{1}{2}\nabla_{\boldsymbol{x}}\Phi^s \cdot \nabla_{\boldsymbol{x}}\Phi^s - \tfrac{1}{2}(1 + \nabla_{\boldsymbol{x}}\zeta \cdot \nabla_{\boldsymbol{x}}\zeta)\left(\Phi^s_z\right)^2 = 0, \end{aligned}\right\} \tag{2.2}$$

where t denotes time, $\Phi^s(\boldsymbol{x}, t) \equiv \Phi(\boldsymbol{x}, \zeta(\boldsymbol{x}, t), t)$ is the free-surface potential, $\Phi^s_z(\boldsymbol{x}, t) \equiv \Phi_z(\boldsymbol{x}, \zeta(\boldsymbol{x}, t), t)$ is the surface vertical velocity, $\nabla_{\boldsymbol{x}} \equiv (\partial/\partial x, \partial/\partial y)$, and g is the acceleration due to gravity. On the side and bottom of the tank, the non-flux condition is imposed:

$$\frac{\partial \Phi}{\partial n} \equiv \Phi_n = 0, \tag{2.3}$$

where n denotes the unit normal to the boundary. As initial conditions, both the free-surface elevation and velocity potential at the initial time $t = 0$ are specified.

For standing waves of period T, we impose an additional condition (in lieu of an initial condition), say:

$$\Phi^s(\boldsymbol{x}, 0) = \Phi^s(\boldsymbol{x}, T/2) = 0, \tag{2.4}$$

corresponding to stationary conditions at $t/T = 0, 0.5, \ldots$.

Unlike a Stokes wave which is steady in a coordinate system moving at its phase speed, standing waves are always unsteady (in time). To investigate the instability of standing waves, we adopt the transition matrix approach (e.g. von Kerczek & Davis 1975) using Floquet theory. The approach is standard and we outline it below for completeness.

We write (2.2) symbolically in terms of a nonlinear operator $\mathscr{N}$:

$$\frac{\partial \boldsymbol{u}}{\partial t} = \mathscr{N}(\boldsymbol{u}), \tag{2.5}$$

where $\boldsymbol{u} = (\zeta(\boldsymbol{x}, t), \Phi^s(\boldsymbol{x}, t))$. In a linear stability analysis, we write $\boldsymbol{u}$ as the sum of a base standing wave $\boldsymbol{u}_0$, satisfying (1)–(4); and a small perturbation $\boldsymbol{u}'$, which satisfies (1) and (3) only:

$$\boldsymbol{u}(\boldsymbol{x}, t) = \boldsymbol{u}_0(\boldsymbol{x}, t) + \boldsymbol{u}'(\boldsymbol{x}, t). \tag{2.6}$$

Substituting (2.6) into (2.5) then gives:

$$\frac{\partial \boldsymbol{u}'}{\partial t} = \mathscr{L}(\boldsymbol{u}'), \tag{2.7}$$

https://doi.org/10.1017/S0022112003006347 Published online by Cambridge University Press

where $\mathscr{L}$ is a time-periodic linearized (variable-coefficient) operator given by the Jacobian of $\mathscr{N}$ with respect to $\boldsymbol{u}$ (evaluated at $\boldsymbol{u}_0$).

For a disturbance with N degrees of freedom, we express the solution of (2.7) as a combination of N linearly independent solutions $\boldsymbol{u}_i'$, $i = 1, \ldots, N$:

$$\boldsymbol{u}' = \sum_{i=1}^{N} \gamma_i \boldsymbol{u}_i', \tag{2.8}$$

where the coefficients γ_i, $i = 1, \ldots, N$, are obtained from the initial condition for $\boldsymbol{u}'$. Using separation of variables, we write:

$$\boldsymbol{u}_i'(\boldsymbol{x}, t) = \sum_{j=1}^{N} \mu_{ij}(t)\psi_j(\boldsymbol{x}), \tag{2.9}$$

where $\psi_j(\boldsymbol{x})$, $j = 1, \ldots, N$, are spatial basis functions and μ_{ij}, $i, j = 1, \ldots, N$, are the time-dependent modal amplitudes.

Substituting (2.8) and (2.9) into (2.7), we obtain an equation involving the $N \times N$ coefficient matrix $\mathscr{U} = [\mu_{ij}]$. Following standard Floquet theory (Coddington & Levinson 1955), we write:

$$\mathscr{U}(t) = \mathscr{P}(t)\exp(\mathscr{C}t), \tag{2.10}$$

where the $N \times N$ matrices $\mathscr{P}$ and $\mathscr{C}$ are, respectively, time-periodic and time-independent. The instability of the flow depends on the eigenvalues λ_j ($j = 1, \ldots, N$) of $\mathscr{C}$: the flow is stable if $\mathrm{Re}(\lambda_j) \leqslant 0$, for all $j = 1, \ldots, N$; and unstable if $\mathrm{Re}(\lambda_j) > 0$, for any $j = 1, \ldots, N$ (the unstable mode is the eigenvector corresponding to λ_j with frequency $\mathrm{Im}(\lambda_j)$).

It is difficult to obtain $\mathscr{C}$ analytically, and we generally resort to a numerical determination from (2.7) of the so-called transition matrix $\mathscr{Q} \equiv \exp(\mathscr{C}T)$. In terms of the eigenvalues σ_j, $j = 1, \ldots, N$ of $\mathscr{Q}$, the eigenvalues of $\mathscr{C}$ are:

$$\lambda_j = \frac{\log \sigma_j}{T}, \qquad j = 1, \ldots, N. \tag{2.11}$$

In practice, given a base flow $\boldsymbol{u}_0$, we obtain the $N \times N$ transition matrix $\mathscr{Q} \equiv [q_{ij}]$ by numerically integrating (2.5) with the initial condition:

$$\boldsymbol{u}_i(\boldsymbol{x}, 0) = \boldsymbol{u}_0(\boldsymbol{x}, 0) + \boldsymbol{u}_i'(\boldsymbol{x}, 0) = \boldsymbol{u}_0(\boldsymbol{x}, 0) + \delta\psi_i(\boldsymbol{x}), \quad \delta \ll 1, \qquad i = 1, \ldots, N, \tag{2.12}$$

to obtain $\boldsymbol{u}_i(\boldsymbol{x}, T)$ and hence $\boldsymbol{u}_i'(\boldsymbol{x}, T)$ (from (6) with $\boldsymbol{u}_0(\boldsymbol{x}, T) = \boldsymbol{u}_0(\boldsymbol{x}, 0)$). Upon using (2.9), we obtain the modal amplitudes μ_{ij} of $\boldsymbol{u}_i'(\boldsymbol{x}, T)$. The process is repeated for each $i = 1, \ldots, N$. The elements of $\mathscr{Q}$ are:

$$q_{ij} = \mu_{ij}(T)/\delta, \qquad i, j = 1, \ldots, N. \tag{2.13}$$

The key to the instability analysis above is the accurate (numerical) evaluation of $\boldsymbol{u}'(\boldsymbol{x}, T) = \boldsymbol{u}(\boldsymbol{x}, T) - \boldsymbol{u}_0$. Hence, two high-accuracy computational capabilities are required: (i) the determination of nonlinear base standing waves $\boldsymbol{u}_0$ satisfying (2.1)–(2.4); and (ii) the integration in time of the nonlinear initial-boundary-value problem (2.1)–(2.3) to obtain $\boldsymbol{u}(\boldsymbol{x}, T)$ given $\boldsymbol{u}(\boldsymbol{x}, 0)$. In this study, we develop an efficient and highly accurate approach based on a high-order spectral element (HOSE) method to accomplish both (i) and (ii).

https://doi.org/10.1017/S0022112003006347 Published online by Cambridge University Press

3. The high-order spectral element (HOSE) method

We seek to solve numerically the evolution of large-amplitude waves in a basin described by the initial boundary-value problem (2.1)–(2.3) plus a certain initial or standing-wave condition (e.g. (2.12) or (2.4)). In the time domain, at each time step, the solution procedure generally consists of two basic steps: (i) given the free-surface elevation ζ and potential Φ^s at time t, solve the nonlinear boundary-value problem of Φ ((2.1) and (2.3)) to obtain the free-surface velocity $\Phi^s_z(t)$; and (ii) given $\Phi^s_z(t)$, integrate the evolution equation, (2.2), forward in time to obtain $\zeta(t+\Delta t)$ and $\Phi^s(t+\Delta t)$ at new time $t+\Delta t$; and the process is repeated. Of the two steps, the computational effort (and hence the resolution) is controlled by step (i) which involves the effects of free-surface nonlinearity and a free-surface domain intersected by the walls of the basin.

A powerful scheme for the simulation of nonlinear surface wave dynamics (for simple free-surface geometry) is the high-order spectral (HOS) method (Dommermuth & Yue 1987). HOS uses a pseudospectral approach, employs global spectral basis functions (wave modes) to represent the wave field, and accounts for their interactions up to high-order M in the wave steepness. HOS obtains exponential convergence with respect to the number of spectral modes N and the order M. In addition, with the use of the fast transform technique bridging the spectral and physical domains, the requisite computational effort of HOS is linearly proportional to N and M. The accuracy and efficiency of HOS allow it to be used for high-resolution computational studies of nonlinear wave–wave and wave–body/bottom interaction mechanisms, for example, long–short wave interactions (Zhang, Hong & Yue 1993), resonant wave interactions with bottom ripples (Liu & Yue 1998), and wave interactions with submerged bodies (Liu, *et al.* 1992; Zhu *et al.* 1999). Owing to the use of global basis functions, however, the application of HOS has been limited to problems with relatively simple boundaries. Direct extension of HOS to problems involving complex boundaries and a surface-piercing wall has not been achieved because of the difficulty in finding appropriate global basis functions, and the poor conditioning of the resulting system (associated with the use of larger numbers say of Chebyshev polynomial modes, see e.g. Canuto *et al.* 1988).

To overcome these difficulties and to retain the merits of HOS, we develop here a high-order spectral element (HOSE) method which is based on the idea of HOS but is now applicable to general nonlinear wave–body problems. Instead of global spectral expansions, in HOSE, we divide the boundary domain into elements and apply spectral expansions over each element using local basis functions. Since global fast transform techniques can no longer be used, the computational effort is increased, but the exponential convergence with respect to the total number of spectral modes (for fixed number of elements) and the interaction order is retained. Significantly, HOSE is useful to problems in complex domains involving surface-piercing bodies.

The formulation and implementation of HOSE are outlined in Appendix A. The accuracy and performance of HOSE have been established through extensive and systematic convergence tests (Zhu 2000). We present here the representative results for the case of nonlinear (standing) waves in a circular tank.

To validate the HOSE method, we show below its convergence with respect to the number of free-surface elements, N_{FE}; the number of Chebyshev modes, N_{Fr}, and the number of Fourier modes, $N_{F\theta}$, within each element; and the number of Fourier/Chebyshev modes employed on the wall and the bottom $N_{w\theta}/N_{wz}$ and $N_{b\theta}/N_{br}$, respectively. Additional convergence results are also shown for the order of the HOSE expansion M, and the time step Δt.

https://doi.org/10.1017/S0022112003006347 Published online by Cambridge University Press

N_{FE}/N_{Fr}	4	8	16
1	7.60×10^{-1}	1.01×10^{-1}	1.10×10^{-4}
2	1.04×10^{-1}	5.93×10^{-4}	3.28×10^{-6}
3	4.04×10^{-2}	3.83×10^{-5}	*
4	1.27×10^{-2}	3.65×10^{-6}	*
8	5.09×10^{-4}	*	*

TABLE 1. Convergence of the normalized maximum error of the vertical velocity on the mean free surface of the standing wave (with wavenumber $k_{3,4}$ and amplitude $A/R = 0.05$) in a circular tank ($h/R = 0.5$) with respect to the number of free-surface elements N_{FE} and the number of free-surface Chebyshev modes N_{Fr}. The symbol * indicates the error to be smaller than 10^{-6} and affected by machine precision limitations. ($N_{F\theta} = N_{w\theta} = N_{b\theta} = 16$, $N_{wz} = N_{br} = 16$.)

First, we show the convergence of the HOSE boundary-value solver itself. To do that, we use the analytic solution of linear standing waves in a circular tank as the benchmark solution:

$$\Phi(r, \theta, z, t) = \frac{A}{\omega_{\ell,\nu}} J_\nu(k_{\ell,\nu} r) \frac{\cosh k_{\ell,\nu}(z+h)}{\cosh k_{\ell,\nu} h} \cos(\ell\theta) \cos(\omega_{\ell,\nu} t), \tag{3.1}$$

where A denotes the wave amplitude, ℓ and ν are non-negative integers representing the wavenumbers in the azimuthal and radial directions, respectively, and J_ν is the νth-order Bessel function of the first kind. In (3.1), the (linear) frequency $\omega_{\ell,\nu}$ is related to the wavenumber $k_{\ell,\nu}$ by the linear dispersion relation: $\omega_{\ell,\nu}^2 = g k_{\ell,\nu} \tanh(k_{\ell,\nu} h)$, where $k_{\ell,\nu}$ is the root of the equation

$$J_\nu'(k_{\ell,\nu} R) = 0, \qquad \ell = 0, 1, \ldots, \quad \nu = 1, 2, \ldots. \tag{3.2}$$

We specify the velocity potential on the mean free surface $\bar{S}_F$ using (3.1) (say at $t = 0$), solve for the vertical velocity Φ_z on $\bar{S}_F$, and compare this to analytic value. For illustration, we consider the standing wave $k_{3,4}$ with amplitude $A/R = 0.05$ in a tank with $h/R = 0.5$. Table 1 shows the maximum error of Φ_z on $\bar{S}_F$. It is computed with fixed numbers of Fourier modes (in the azimuthal direction) on the free surface ($N_{F\theta} = 16$) and the sidewall and bottom of the tank ($N_{w\theta} = N_{b\theta} = 16$), and numbers of Chebyshev modes on the sidewall and bottom of the tank ($N_{wz} = N_{br} = 16$), but varying the number of free-surface elements N_{FE} and the number of free-surface Chebyshev modes N_{Fr}. As expected, for fixed (and sufficient) N_{FE}, we observe exponential convergence with N_{Fr}; while for fixed N_{Fr}, rapid convergence with N_{FE} is obtained. (For a detailed description of these numerical parameters, see Appendix A.3).

Table 2 shows similar convergence test results obtained by varying N_{wz} and N_{br} with fixed $N_{FE} = N_{Fr} = 8$ and $N_{F\theta} = N_{w\theta} = N_{b\theta} = 16$. For fixed (and sufficient) N_{br}, exponential convergence with N_{wz} is again obtained. For a fixed N_{wz}, on the other hand, the results do not further converge with increasing N_{br} since, for this relatively deep ($h/R = 0.5$) case, further resolution on the tank bottom has little effect on the free-surface velocity we consider.

We now consider the convergence of HOSE with the interaction order M, as well as with respect to the time integration. To do this, we address a problem involving nonlinear time evolution. We choose the problem of determining the finite-amplitude

https://doi.org/10.1017/S0022112003006347 Published online by Cambridge University Press

N_{br}/N_{wz}	4	8	12
4	5.36×10^{-3}	1.91×10^{-5}	1.15×10^{-6}
8	5.35×10^{-3}	2.06×10^{-5}	1.21×10^{-6}
16	5.35×10^{-3}	2.05×10^{-5}	1.22×10^{-6}

TABLE 2. Convergence of the normalized maximum error of the vertical velocity on the mean free surface of the standing wave (with wavenumber $k_{3,4}$ and amplitude $A/R = 0.05$) in a circular tank ($h/R = 0.5$) with respect to the numbers of Chebyshev modes on the sidewall and bottom of the tank N_{wz} and N_{br}. ($N_{FE} = N_{Fr} = 8$ and $N_{F\theta} = N_{w\theta} = N_{b\theta} = 16$.)

M/N_{FE}	1	2	4	8
1	1.00000	1.00000	1.00000	1.00000
2	1.04388	0.99953	0.99938	0.99938
3	1.04387	0.99897	0.99881	0.99881
4	1.04387	0.99896	0.99880	0.99880

TABLE 3. Nonlinear frequency $\Omega_{0,6}$ (normalized by its linearized value $\omega_{0,6}$) of a nonlinear axisymmetric standing wave with wavenumber $k_{0,6}$ in a circular tank, obtained using varying numbers of free-surface elements N_{FE} and order M. ($N_{Fr} = 8$, $N_{F\theta} = N_{w\theta} = N_{b\theta} = 16$, $N_{wz} = N_{br} = 16$, $T/\Delta t = 128$, $h/R = 0.5$.)

standing waves in a circular tank (the procedure for finding the nonlinear standing wave configuration using HOSE computations is given in Appendix B).

For reference, we denote the nonlinear frequency of a nonlinear standing wave in a circular tank with wavenumber $k_{\ell,v}$ by $\Omega_{\ell,v}$. Since $\Omega_{\ell,v}$ has a direct dependence on the wave amplitude (see e.g. Tsai & Yue 1987), we here fix the amplitude of the standing wave: $A \equiv (\zeta_{\max} - \zeta_{\min})/2 = 0.016R$, and consider the convergence of $\Omega_{\ell,v}$ with respect to M and the time step Δt of the simulations. Table 3 shows the case for $\Omega_{0,6}$ with $N_{Fr} = 8$, $N_{F\theta} = N_{w\theta} = N_{b\theta} = 16$, $N_{wz} = N_{br} = 16$, and $T/\Delta t = 128$. When the nonlinear effects are included ($M > 1$), the value of of $\Omega_{0,6}$ is, as known, smaller than that for the linear standing wave ($M = 1$): $\omega_{0,6} = [gk_{0,6}\tanh(k_{0,6}h)]^{1/2}$. For fixed N_{FE}, we obtain exponential convergence for $\Omega_{0,6}$ with respect to M; while for a fixed M, rapid convergence with N_{FE} is achieved.

For the time integration of the evolution equations in HOSE, we employ a fourth-order Runge–Kutta scheme. The error in the time integration for $T \sim 1$ is thus expected to be $O(\Delta t/T)^4$ (e.g. Dommermuth & Yue 1987). Table 4 displays the convergence of $\Omega_{0,6}$ with respect to $T/\Delta t$ and the order M. For these computations, the other parameters are fixed: $N_{FE} = N_{Fr} = 8$, $N_{F\theta} = N_{w\theta} = N_{b\theta} = 16$, and $N_{wz} = N_{br} = 16$. For these typical computational parameters, and $T/\Delta t = 128$, $\Omega_{0,6}$ converges to at least five decimal places at any order M.

We show also the convergence with respect to standing-wave profiles. Figure 1 plots the radial profile of the axisymmetric standing wave $k_{0,6}$ at $t = 0$ (corresponding to maximum elevation of this standing-wave profile at the origin). The results are obtained with different N_{FE} and N_{Fr} but fixed $M = 3$, $N_{F\theta} = N_{w\theta} = N_{b\theta} = 16$, $N_{wz} = N_{br} = 16$, and $T/\Delta t = 128$. The results converge rapidly with increasing N_{FE} and N_{Fr}. In particular, for $N_{FE} = 4$, the profiles obtained using $N_{Fr} = 8$ and 16 are graphically indistinguishable.

https://doi.org/10.1017/S0022112003006347 Published online by Cambridge University Press

$M/T/\Delta t$	16	32	64	128
1	1.00000	1.00000	1.00000	1.00000
2	0.99919	0.99936	0.99938	0.99938
3	0.99861	0.99879	0.99881	0.99881
4	0.99861	0.99879	0.99880	0.99880

TABLE 4. Nonlinear frequency $\Omega_{0,6}$ (normalized by its linearized value $\omega_{0,6}$) of a nonlinear axisymmetric standing wave with wavenumber $k_{0,6}$ in a circular tank, obtained using varying time step sizes $T/\Delta t$ and the order M. ($N_{FE} = N_{Fr} = 8$, $N_{F\theta} = N_{w\theta} = N_{b\theta} = 16$, $N_{wz} = N_{br} = 16$, $h/R = 0.5$.)

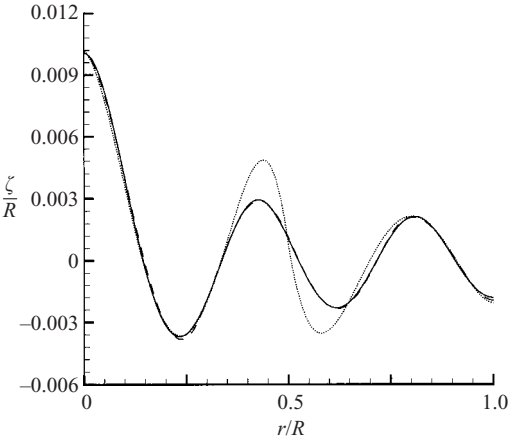


FIGURE 1. Free-surface profiles of nonlinear axisymmetric standing wave $k_{0,6}$ in a circular tank at $t = 0$ (corresponding to maximum elevation of this standing wave profile at the origin) obtained with: ···, $(N_{FE}, N_{Fr}) = (2, 4)$; – – –, (4, 4); —·—, (4, 8); —, (4, 16). The wave amplitude $A/R = 0.01$. ($M = 3$, $N_{F\theta} = N_{w\theta} = N_{b\theta} = 16$, $N_{wz} = N_{br} = 16$, $T/\Delta t = 128$, $h/R = 0.5$.)

Figure 2 shows similar convergence results of the free-surface profile for the non-axisymmetric standing wave $k_{2,5}$ at $t = 0$. Plotted are the radial profiles along $\theta = 0$ and azimuthal profiles on the wall (at $r = R$). They are computed with varying N_{Fr} but fixed $M = 3$, $N_{FE} = 4$, $N_{F\theta} = N_{w\theta} = N_{b\theta} = 16$, $N_{wz} = N_{br} = 32$ and $T/\Delta t = 128$. The wave profiles are seen to converge rapidly with increasing N_{Fr}. As in the case in figure 1, the wave profiles obtained with $N_{Fr} = 8$ and 16 are graphically indistinguishable. Note that the profiles (with $M = 3$) in figures 1 and 2 converge with the corresponding results obtained with $M = 4$ to at least five decimal places.

As a final validation of this problem, we compare the present HOSE result (with $M = 3$) for $\Omega_{0,2}$ with the fully nonlinear result of Tsai & Yue (1987). The comparison is plotted in figure 3 for a broad range of standing-wave amplitudes (up to $A/R \sim 0.2$; the value for the maximum steepness of this type of wave is not known). Excellent agreement (to within 1% for $1 - \Omega_{0,2}/\omega_{0,2}$) between the present result (converged to five decimal places with $M = 3$) and that of Tsai & Yue (1987) is obtained for the range shown.

https://doi.org/10.1017/S0022112003006347 Published online by Cambridge University Press

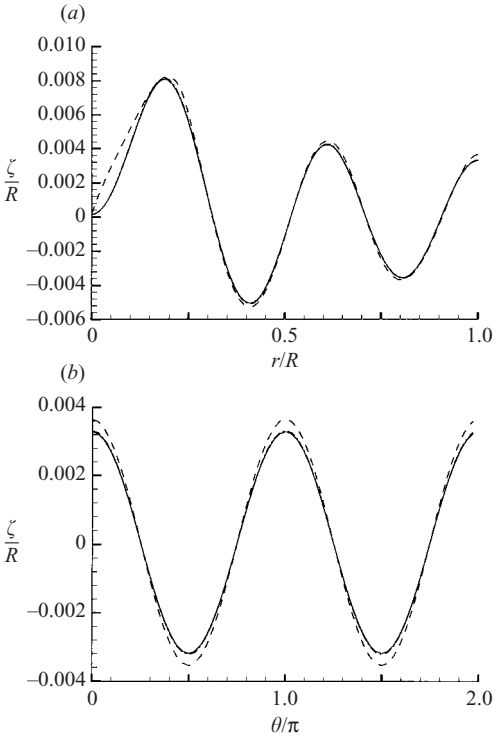


FIGURE 2. (*a*) Radial and (*b*) azimuthal free-surface profiles of nonlinear non-axisymmetric standing wave $k_{2,5}$ in a circular tank at $t = 0$ (corresponding to maximum elevation of this standing wave profile at $r = 0.19R$, $\theta = 0$) on (*a*) $\theta = 0$ and (*b*) $r = R$. The results are obtained with – – –, $N_{Fr} = 4$; —·—, 8; and —, 16. The wave amplitude $A/R = 0.008$. ($M = 3$, $N_{FE} = 4$, $N_{F\theta} = N_{w\theta} = N_{b\theta} = 16$, $N_{wz} = N_{br} = 32$, $T/\Delta t = 128$, $h/R = 0.5$.)

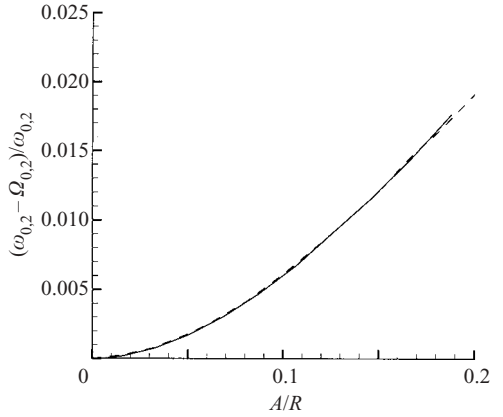


FIGURE 3. Frequency $\Omega_{0,2}$ of nonlinear axisymmetric standing wave $k_{0,2}$ in a circular tank (with $h/R = 1.0$), normalized by $\omega_{0,2} = (gk_{0,2}\tanh k_{0,2}h)^{1/2}$, as a function of the wave amplitude A/R. – – –, fully nonlinear result of Tsai & Yue (1987); —, present HOSE simulation (with $M = 3$).

https://doi.org/10.1017/S0022112003006347 Published online by Cambridge University Press

4. Numerical results

We apply the transition matrix method using HOSE computations to study the two- and three-dimensional instability of finite-amplitude standing waves in rectangular and circular tanks.

4.1. *Instability of plane standing waves*

We consider the stability of finite-amplitude plane standing waves to small two- and three-dimensional disturbances. The two-dimensional instability problem has been investigated by MR. Pierce & Knobloch (1994) considered the three-dimensional instability problem, but restricted their attention to long modulational transverse disturbances. Since the present work is based on direct HOSE computations, we consider only finite wavelength disturbances, and our findings cannot be compared with their results.

As a validation, we first revisit the two-dimensional case, comparing our results to those of MR for small to moderate wave steepness. We then study the more general three-dimensional instability problem.

4.1.1. *Two-dimensional instability*

As in MR, we consider here the deep-water case. We choose a computational domain containing 8 fundamental standing waves, wavenumber k, and consider two-dimensional perturbations given by Fourier series with components $\mathrm{e}^{\mathrm{i}pkx/8}$, $p = 0, 1, \ldots, N$. Note that the choice of computational domain allows us to consider disturbances with wavelength up to eight times that of the base standing wave. In the HOSE simulations, we use $M = 3$ and 5, $N_{FE} = 1$, $N_F = 512$ (64 Fourier spectral modes per fundamental wavelength), $T/\Delta t = 128$ and $N = 32$. These computational parameters obtain results for growth rates of the perturbation modes convergent to the fourth decimal place.

Following § 2, we obtain the eigenvalues λ_j and eigenvectors $\boldsymbol{V}^j = v_p^j$, $j, p = 0, 1, \ldots, N$, of the problem. For convenience, we label these eigenmodes by the number(s) of their dominant Fourier component(s), for example, mode '(p)' corresponds to that mode (j) wherein the pth component $|v_p^j|$ is dominant (maximum). In many cases, $\boldsymbol{V}^j$ contains a pair of equally dominant components, say, p_1, p_2, in which case it is more meaningful to refer to this mode as '(p_1, p_2)'.

Figure 4 plots, as a function of wave steepness kA of the base standing wave, eigen-frequencies $\mathrm{Im}(\lambda)$ of the transition matrix and the growth rates $\mathrm{Re}(\lambda)$ of the unstable modes. The present HOSE predictions ($M = 3$ and 5) are compared to those of MR. The comparisons are good for small to moderate values of $kA <\sim 0.25$. (As a reference, according to MR, the possible maximum steepness of a plane standing wave is $(kA)_{\max} \simeq 0.62$). As kA increases further, HOSE predictions begin to deviate from the fully nonlinear MR results and more so for $M = 3$ than $M = 5$, as expected. Figure 4 provides a guideline for the use of HOSE in this section (in terms of kA and M). Comparing figures 4(a) and 4(b), we see that the occurrence of instability corresponds to the coalescence of pairs of eigenmodes. For instance, the eigen-frequencies associated with modes (7) and (9) converge into a single value at $kA \approx 0.092$, resulting in an unstable mode (7, 9).

From figure 4, we see that the unstable modes consist of sideband and superharmonic disturbances, (7, 9) and (6, 10), and (14, 22), respectively. For (14, 22), stability is reestablished at $kA \simeq 0.28$. From MR, it is known that (7, 9) and (6, 10) eventually also restabilize, but at larger kA beyond the scope of the present simulation.

https://doi.org/10.1017/S0022112003006347 Published online by Cambridge University Press

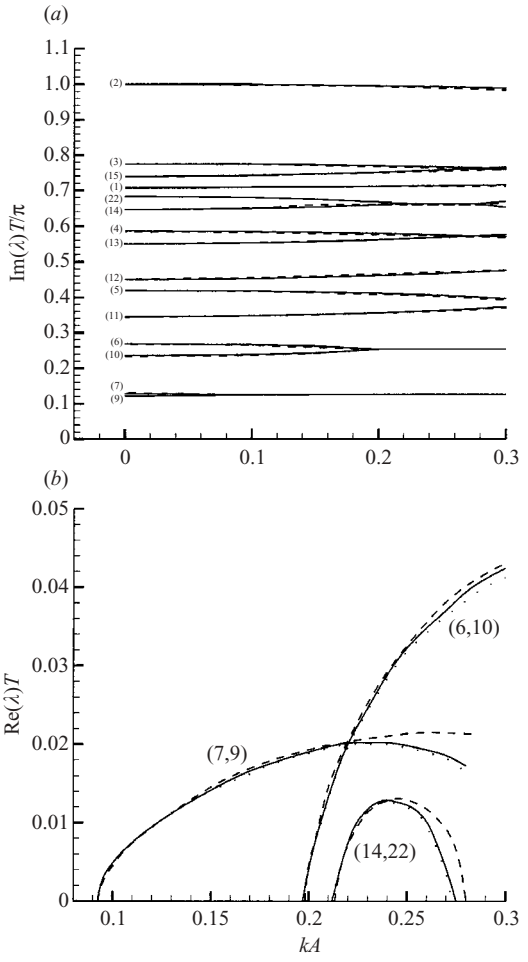


FIGURE 4. (*a*) Eigen-frequency Im(λ) and (*b*) growth rate Re(λ) of two-dimensional disturbances on a plane standing wave as a function of wave steepness kA. The eigenmodes are labelled by their dominant Fourier component(s). The results plotted are the present HOSE results with $M = 3$ ($\cdots$) and $M = 5$ (—) and the fully nonlinear results of Mercer & Roberts (1992) (– – –). (The HOSE results with $M = 3$ and $M = 5$ in (*a*) are graphically indistinguishable.)

4.1.2. *Three-dimensional instability*

We now turn to the instability of plane standing waves to three-dimensional disturbances. We consider a base plane standing wave of wavenumber k (in the x-direction), and introduce three-dimensional disturbances described by Fourier series with components $e^{ik(px/\mathscr{L}+qy/\mathscr{W})}$, $p, q, = 0, 1, \ldots$. To ensure double spatial periodicity (in the x- and y-directions) for both the base flow and disturbances, $\mathscr{L}$ must be rational while $\mathscr{W}$ is arbitrary.

We conduct systematic computations (with $M = 5$, $N_{FE} = 1$, $N_F = 256 \times 256$, and $T/\Delta t = 128$) for the range of $kA < \sim 0.3$, which is about 50% of the maximum steepness of plane standing waves (e.g. MR). From these computations, we find that a plane standing wave is unstable to three-dimensional perturbations for any (rational) $\mathscr{L}$. In particular, the unstable three-dimensional disturbance ($q \neq 0$) contains

https://doi.org/10.1017/S0022112003006347 Published online by Cambridge University Press

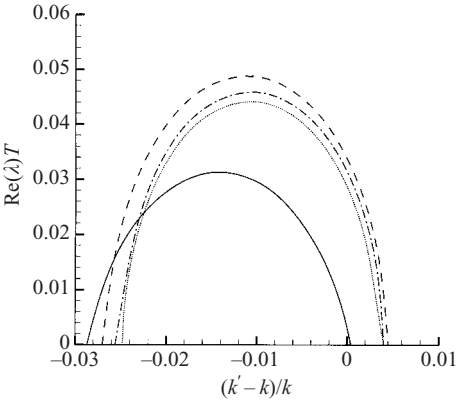


FIGURE 5. Growth rate of the three-dimensional unstable mode as a function of the wavenumber of the disturbance k' for a plane standing wave of wave steepness $kA = 0.20$. The plotted are the results for the disturbance with ···, direction $\alpha = 90°$; —·—, 75°; – – –, 60°; —, 41°, corresponding to $\mathscr{L} = 4$ and $\mathscr{W}$, $p, q = 4/7^{1/2}$, 3, 1; $2/3^{1/2}$, 2, 1; $4/15^{1/2}$, 1, 1; and 4, 0, 4, respectively.

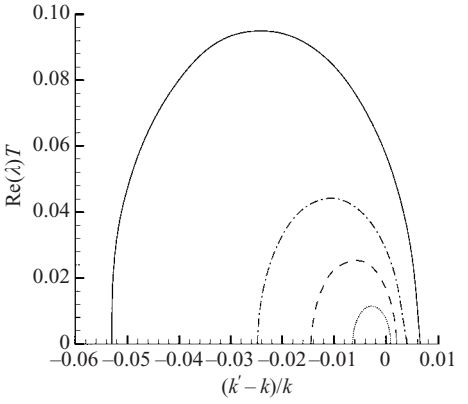


FIGURE 6. Growth rate of a transverse ($\alpha = 90°$) unstable mode on a plane standing waves of ···, wave steepness $kA = 0.10$; – – –, 0.15; —·—, 0.20; and —, 0.30.

a dominant Fourier component satisfying $k'/k \equiv ((p/\mathscr{L})^2 + (q/\mathscr{W})^2)^{1/2} \simeq 1$. The crest line of this mode is oblique to the base standing wave at an angle $\alpha = \tan^{-1}(q\mathscr{L}/p\mathscr{W})$.

For example, for $\mathscr{L} = 4$, the plane standing wave is unstable to the three-dimensional disturbances with $\mathscr{W}$, $p, q = 4/7^{1/2}$, 3, 1; $2/3^{1/2}$, 2, 1; $4/15^{1/2}$, 1, 1; and 4, 0, 4, which correspond to crest angles $\alpha = 41°$, 60°, 75° and 90°, respectively. Figure 5 shows the growth rate of these modes in the neighbourhood of the critical point $k'/k = 1$. The wave steepness of the base plane standing wave is $kA = 0.20$. The maximum growth rate generally obtains with $k' < k$. As we shall see, this is explained in terms of the nonlinear versus linear dispersion relationships for plane standing waves.

To investigate the dependence of the instability on kA, we plot in figure 6 the growth rates of the transverse ($\alpha = 90°$) unstable mode for different values of kA. This mode is unstable near $k'/k = 1$ for any kA. From the figure, we see that both the region of instability and the maximum value of the growth rate increase as kA increases.

https://doi.org/10.1017/S0022112003006347 Published online by Cambridge University Press

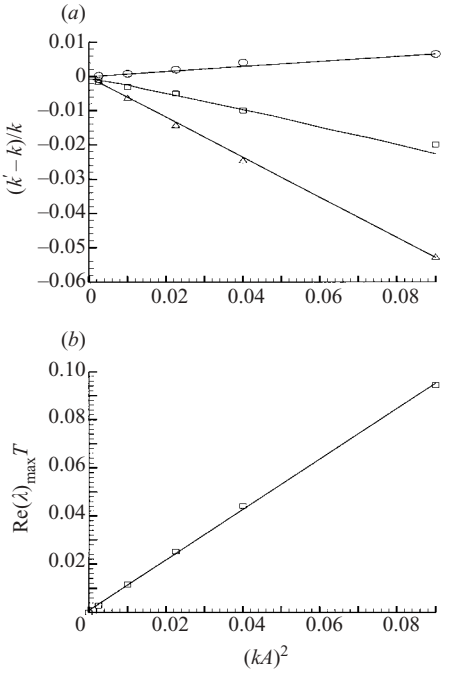


FIGURE 7. Dependence of (*a*) the upper (k_+: ○) and lower (k_-: △) values of the unstable regions, and the values (k_m: □) at which maximum growth rates obtain; and (*b*) the maximum values of the growth rate (□); on the wave steepness of the base standing wave kA, for the case of figure 6. Also plotted are the best linear fits to k_+ and k_- in (*a*), the quantity Ω^2/g in (*a*), and the best linear fit to the maximum growth rate in (*b*).

To better understand the dependence on kA of the size of the unstable region and maximum value of the growth rate in figure 6, we plot, in figure 7(*a*), the upper (k_+) and lower (k_-) values of k' marking the instability region, as a function of $(kA)^2$. The computational results are fitted closely by linear relations between $(k_\pm - k)/k$ and $(kA)^2$. Figure 7(*b*) plots the maximum growth rate also as a function of $(kA)^2$. The quadratic dependence on kA is again evident.

Finally, we plot the value $k' = k_m$ at which the maximum growth rate is obtained (figure 7*a*). As seen from the figure, $k_m \simeq \Omega^2/g$ where Ω is the nonlinear frequency of the base standing wave. This also implies that the frequency of the most unstable mode satisfies $\omega' \equiv \sqrt{k'g} \simeq \Omega$, i.e. the most unstable mode is the one which has the same frequency as the base standing wave in this case.

The essential features of these three-dimensional instability results are captured in a simple analysis. For simplicity, we consider a base flow given by the linear standing wave solution: $\zeta_0 = A\cos(kx)\cos\omega t$ and $\phi_0 = -(gA/\omega)\cos(kx)\exp(kz)\sin\omega t$; $k = \omega^2/g$. Consider, as a special case, a disturbance mode perpendicular to the base standing wave: $\zeta' = \tilde{\zeta}(t)\cos k'y$ and $\phi' = \tilde{\phi}(t)\cos k'y\exp(k'z)$, where $\tilde{\zeta}(t)$ denotes the free-surface elevation of the small disturbance while $\tilde{\phi}(t)$ is the amplitude of the associated disturbance potential. Upon substituting the total free-surface elevation $\zeta = \zeta_0 + \zeta'$ and velocity potential $\Phi = \phi_0 + \phi'$ into (2.2), we obtain the linearized evolution equations for the disturbance:

$$\tilde{\zeta}_t - \left[1 + \tfrac{1}{2}(kA)^2\cos^2\omega t\right]k\tilde{\phi} = 0, \qquad \tilde{\phi}_t + g\tilde{\zeta} = 0. \tag{4.1}$$

https://doi.org/10.1017/S0022112003006347 Published online by Cambridge University Press

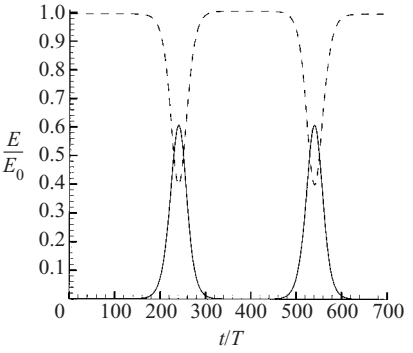


FIGURE 8. Time history of total wave energy E (normalized by the initial energy of the fundamental wave E_0) during nonlinear evolution of a plane standing wave $kA = 0.20$ initially disturbed by an unstable transverse perturbation (with $\mathscr{L} = 4$, $\mathscr{W} = 4.04$, $p = 0$, $q = 4$) for: – – –, the fundamental standing wave; —, the transverse mode.

Combining (4.1), we obtain:

$$\tilde{\phi}_{tt} + gk'\left[1 + \tfrac{1}{4}(kA)^2 + \tfrac{1}{4}(kA)^2 \cos 2\omega t\right]\tilde{\phi} = 0. \tag{4.2}$$

Upon introducing a non-dimensional time $\tau = 2\omega t$, (4.2) is rewritten in a standard form of the Mathieu equation (e.g. Bender & Orszag 1978):

$$\tilde{\phi}_{\tau\tau} + (a + 2b\cos\tau)\tilde{\phi} = 0, \tag{4.3}$$

where $a = gk'[1+(kA)^2/4]/(4\omega^2)$ and $b = gk'(kA)^2/(8\omega^2)$. It is known that the solution of (4.3) is unstable in the neighbourhood of $a = 1/4$ with growth rate proportional to b. These correspond to $k'/k = [1+(kA)^2/4]^{-1} = 1 + O(kA)^2$ and growth rate $\propto (kA)^2$. These results from linearized analysis express the salient features of figures 6 and 7.

The three-dimensional instability we find here is consistent with the class Ia instability of propagating short-crested waves in the standing-wave limit (Ioualalen & Kharif 1994). An extension of their result to the two-dimensional standing-wave limit implies the existence of the transverse instability we find. Because of the unsteadiness of standing waves, however, general features of this instability cannot be obtained from the quasi-steady analysis of propagating waves.

4.1.3. *Long-time evolution*

For progressive Stokes waves, it is known that, because of instability, long-time simulations using model equations such as the nonlinear Schrödinger (NLS) equation lead to recurrence (e.g. Yuen & Ferguson 1978). To see if such phenomenon might obtain in the present case, we perform long-time HOSE simulations of a finite-amplitude plane standing wave initially perturbed by an unstable mode. For specificity, we consider a base flow with $kA = 0.20$ initially perturbed by a transverse unstable mode with $p = 0$ and $k'/k = q/\mathscr{W} = 0.99$. We perform HOSE simulations (with $M = 5$, $N_{FE} = 1$, $N_F = 256 \times 256$, $T/\Delta t = 128$) up to $t = 700T$.

For this case, we can decompose the total (potential plus kinetic) energies of the base standing wave and the transverse disturbance. Figure 8 plots the time variations of these, showing a clear long-time recurrence (of period $\sim 300T$). At its maxima (at $t/T \simeq 240$ and 540), the transverse mode has an energy that exceeds that of the longitudinal wave (corresponding to 60% of the total initial energy). Between these maxima, the initial state is completely recovered.

https://doi.org/10.1017/S0022112003006347 Published online by Cambridge University Press

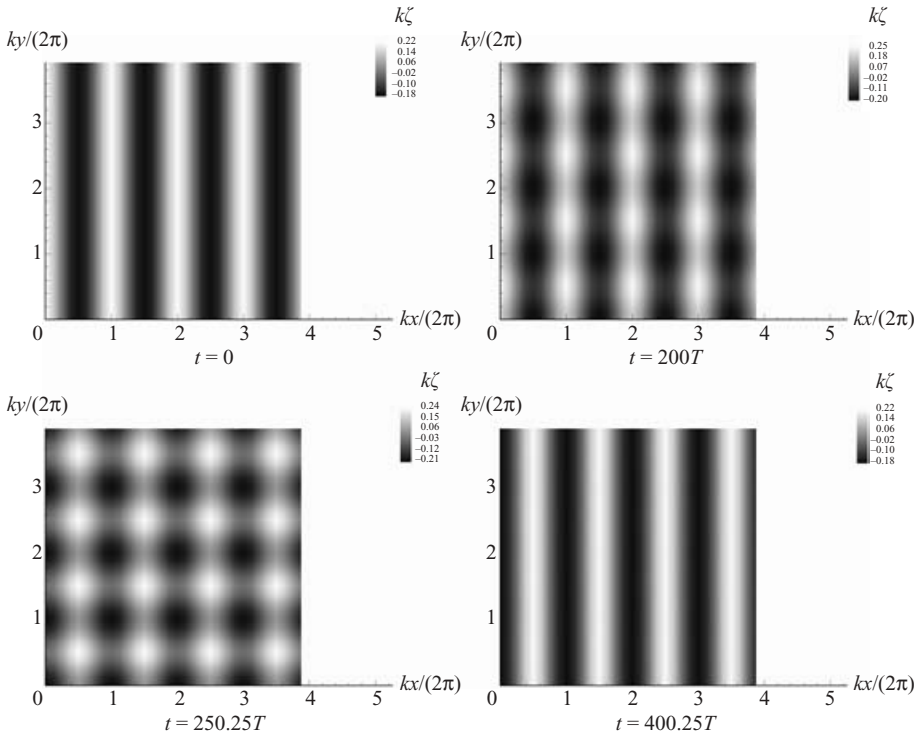


FIGURE 9. Snapshots of the free surface during the nonlinear evolution of a plane standing wave $kA = 0.20$ initially perturbed by an unstable transverse wave (with $\mathscr{L} = 4$, $\mathscr{W} = 4.04$, $p = 0$, $q = 4$).

Figure 9 shows the free-surface wave patterns at several stages of this evolution cycle. At $t = 0$, the free surface is dominated by the longitudinal base standing wave. At $t = 200T$, an interference pattern obtains as a result of the growing transverse mode. At $t \simeq 250T$, the energies of the two modes are comparable, resulting in a distinct checker-board pattern. Finally, at $t \simeq 400T$, the free surface returns to a two-dimensional pattern very similar to the initial wave field.

Unlike the NLS, the present long-time predictions are not limited by cascade of energy to increasingly higher wavenumbers. However, the effect of damping due to viscosity in the physical problem should still be accounted for. For water waves inside a tank, the dominant viscous effect arises from the boundary layer near the solid boundary. The average damping rate is $D \sim \nu^{1/2} L^{-3/4}/(ng)^{1/4}$ (e.g. Mei 1983), where L is the characteristic length of the tank, n the number of waves in the tank, and ν the kinematic viscosity. Using this for a single standing wave in the tank, and the recurrence time above, we estimate that the recurrence phenomenon will be affected by viscous damping for $L < \sim 0.5\,\mathrm{m}$.

4.2. *Instability of standing waves in a circular tank*

We consider the three-dimensional instability of standing waves in a circular tank, radius R and mean water depth h. For a base (large-amplitude) standing wave with wavenumber $k_{\ell,\nu}$ (azimuthal wavenumber ℓ and radial wavenumber ν), we investigate its stability to three-dimensional perturbations given by Fourier–Bessel series with

https://doi.org/10.1017/S0022112003006347 Published online by Cambridge University Press

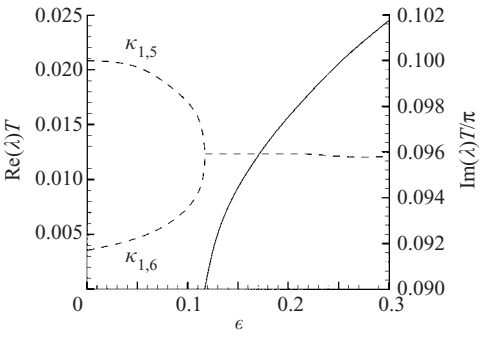


FIGURE 10. —, growth rate $\mathrm{Re}(\lambda)$ and – – –, eigen-frequency $\mathrm{Im}(\lambda)$ of the perturbation containing $(\kappa_{1,5}, \kappa_{1,6})$ for the axisymmetric standing wave $k_{0,6}$ in a circular tank ($h/R = 0.5$) as a function of the fundamental wave steepness ε.

components:

$$J_\nu(\kappa_{\ell,\nu} r)\mathrm{e}^{\mathrm{i}\ell\theta}, \quad \ell = 0, 1, \ldots; \quad \nu = 1, 2, \ldots \tag{4.4}$$

Hereinafter, to avoid possible confusion, we use k for the wavenumber of the base standing wave and κ for the wavenumber of each component of a perturbation although numerically $k_{\ell,\nu} = \kappa_{\ell,\nu}$.

The unstable mode generally contains multiple dominant wavenumber components, each with its own wavenumber. For plane unstable modes, we use the standard notation, (p_1, p_2), to represent an unstable mode with dominant components of wavenumbers p_1 and p_2. For the three-dimensional problem, each of the dominant components in an unstable mode has a wavenumber which is two-dimensional, and the mode might be represented by a sequence of ordered pairs $\{(\ell, \nu)_1, (\ell, \nu)_2, \ldots\}$, say. To avoid the possible confusion of (ℓ, ν) here with the (p_1, p_2) above, we use the notation $\kappa_{\ell,\nu}$ instead for the dominant wavenumber component $((\ell, \nu))$.

Hereunder, we consider separately the case of axisymmetric ($\ell = 0$) and non-axisymmetric ($\ell > 0$) base standing waves. For specificity, we set $h/R = 0.5$, and in the HOSE computations, use: $M = 3$, $N_{FE} = 16$, $N_{F\theta} = N_{w\theta} = N_{b\theta} = 64$, $N_{Fr} = 8$, $N_{wz} = N_{br} = 32$, and $T/\Delta t = 128$.

4.2.1. *Axisymmetric standing waves*

We perform systematic computations for $\ell = 0$ and $\nu = 1, \ldots$ for a range of base wave steepness ε, defined as $\varepsilon \equiv |\nabla\zeta|_{max}$ (at $t = 0$). The stability analysis results are summed up as follows: the axisymmetric standing wave is unstable to three-dimensional disturbances for all ν (we computed to beyond $\nu = 7$) when ε exceeds some threshold value ε_c (function of ν for a given h/R). The (most) unstable mode contains a pair of dominant components: $(\kappa_{1,\nu}, \kappa_{1,\nu-1})$.

The instability here resembles that of plane standing waves (cf. § 4.1.1). In figure 10, we present a typical result for the variation of the eigen-frequency and growth rate as ε increases from zero to beyond ε_c. The result is obtained for the axisymmetric wave $k_{0,6}$. When $\varepsilon < \varepsilon_c$, the eigen-frequencies of two perturbations, with (dominant) components $\kappa_{1,5}$ and $\kappa_{1,6}$, respectively, differ and the fundamental wave is stable. When $\varepsilon > \varepsilon_c$ ($\simeq 0.12$ in this case), the eigen-frequencies of these two modes coalesce, and the base wave becomes unstable (indicated by a positive growth rate in figure 10) to the perturbation containing these as dominant components.

https://doi.org/10.1017/S0022112003006347 Published online by Cambridge University Press

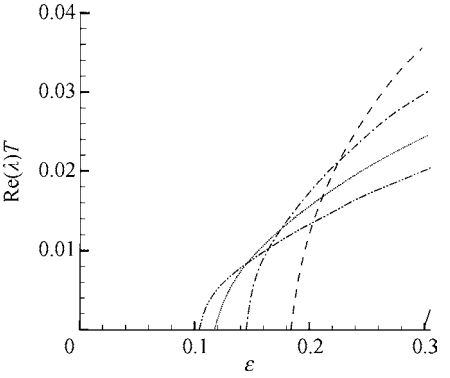


FIGURE 11. Growth rates of the perturbation containing $(\kappa_{1,\nu}, \kappa_{1,\nu-1})$ for axisymmetric standing waves $k_{0,\nu}$ in a circular tank $(h/R = 0.5)$ as a function of the fundamental wave steepness ε. The plotted curves are for: —, $\nu = 3$; – – –, $\nu = 4$; —·—, $\nu = 5$; · · ·, $\nu = 6$; —· ·—, $\nu = 7$.

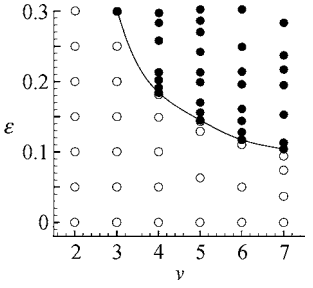


FIGURE 12. Region of (in)stability for axisymmetric standing waves $k_{0,\nu}$ as a function of ν and fundamental wave steepness ε. ○, stable; ●, unstable standing waves.

Similar results obtain for other values of ν. Figure 11 plots the growth rates for $\nu = 3$ to 7 as a function ε. For a given ν, we see that the growth rate becomes positive and increases monotonically with ε beyond some critical steepness ε_c. The value of ε_c depends on ν and generally decreases as ν increases.

Figure 12 plots the region of instability in the (ε, ν)-plane for axisymmetric base standing waves. ε_c decreases as the radial wavenumber ν increases resulting in a upward concave stability boundary. This feature bears a resemblance to a different but related problem in which axisymmetric waves propagating radially from a heaving hemisphere develop an instability resulting in a distinct three-dimensional wave pattern (Tatsuno, Inoue, & Okabe 1969).

4.2.2. *Non-axisymmetric waves*

Extensive computations and stability analyses are performed also for non-axisymmetric base standing waves for varying ℓ, ν and ε. Similar to axisymmetric standing waves, non-axisymmetric standing waves with azimuthal mode number $\ell \geqslant 1$ (we calculated them to beyond $\ell = 3$) are found to be unstable to three-dimensional perturbations beyond a certain critical base wave steepness $\varepsilon > \varepsilon_c$, where ε_c depends on ℓ and ν (for given h/R). For $\ell = 1$, the unstable perturbation is a single mode containing a pair of dominant Fourier–Bessel components: $\kappa_{0,\nu}$ and $\kappa_{0,\nu+1}$. For $\ell > 1$, the situation is more complex and involves two unstable modes with pairs of dominant Fourier–Bessel components: $(\kappa_{\ell-1,\nu+1}, \kappa_{\ell+1,\nu-1})$ and $(\kappa_{\ell-1,\nu}, \kappa_{\ell+1,\nu})$,

https://doi.org/10.1017/S0022112003006347 Published online by Cambridge University Press

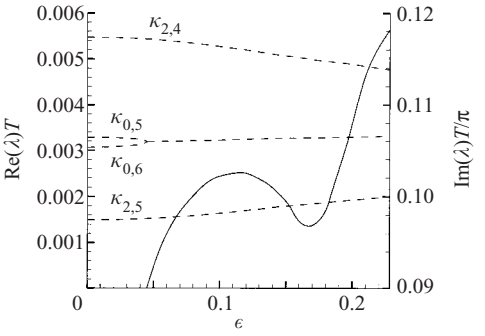


FIGURE 13. —, growth rate Re(λ) and – – –, eigen-frequency Im(λ) of three-dimensional perturbations (labelled by their respective dominant components) for a non-axisymmetric base standing wave, wavenumber $k_{1,5}$, in a circular tank ($h/R = 0.5$) plotted as a function of fundamental wave steepness ε.

respectively. Depending on the base wave ℓ and ν, the values of the critical steepness ε_c for these modes are generally close but not identical.

Figure 13 shows a typical $\ell = 1$ result for the case of a base standing wave with wavenumber $k_{1,5}$. The eigen-frequency and growth rate of the unstable mode are plotted as a function of ε. The results are qualitatively similar to the axisymmetric case: beyond a certain ε_c, the eigen-frequencies of two separate (stable) modes with dominant components $\kappa_{0,5}$ and $\kappa_{0,6}$, respectively, coalesce forming a single unstable mode containing these dominant components. The growth rate of this unstable mode depends on increasing $\varepsilon > \varepsilon_c$ in a non-monotonic fashion in contrast to the axisymmetric cases (cf. figures 10 and 11). Analysing the components of the unstable mode, it is found that, for $\varepsilon > \sim 0.17$, two additional components, $\kappa_{2,4}$ and $\kappa_{2,5}$ (corresponding to $\kappa_{\ell+1,\nu-1}$ and $\kappa_{\ell+1,\nu}$), begin to grow in amplitude, and eventually become co-dominant (with $\kappa_{0,5}$ and $\kappa_{0,6}$) for $\varepsilon \geqslant 0.20$.

For $\ell > 1$, the results differ qualitatively. In this case, two unstable perturbations are found, each containing a pair of dominant components, ($\kappa_{\ell-1,\nu+1}$, $\kappa_{\ell+1,\nu-1}$) and ($\kappa_{\ell-1,\nu}$, $\kappa_{\ell+1,\nu}$). Figure 14 shows the results, as a function of ε, for two non-axisymmetric base standing-wave cases: $k_{2,5}$ and $k_{3,5}$. In each case, the two unstable modes are plotted. For each of the modes, as ε approaches ε_c, instability is initiated by the merging of the eigen-frequencies of two separate modes (with different dominant components) to form a single unstable mode containing both the dominant components. For each base standing wave, the critical steepnesses of the unstable modes are generally close and the growth rate behaviours are qualitatively similar with strong evidence of the re-establishment of stability for large ε. We note that for the cases we consider, for given ν, the critical steepness ε_c increases with ℓ (cf. figures 13 and 14).

To help visualize the features of the instabilities, in figure 15, we show the instantaneous free-surface patterns for three sample cases. The figure shows, for example, how an initially axisymmetric base standing wave (wavenumber $k_{0,4}$) loses its axisymmetry as the dominant unstable mode (with wavenumber components $\kappa_{1,3}$, $\kappa_{1,4}$) develops, case I. Similarly, a non-axisymmetric base standing wave (wavenumber $k_{1,5}$) will, depending on its initial steepness (see figure 13), develop into an axisymmetric standing wave (with dominant components $\kappa_{0,5}$, $\kappa_{0,6}$), case II; or a non-axisymmetric standing wave with higher azimuthal wavenumber (with dominant components $\kappa_{2,4}$, $\kappa_{2,5}$), case III.

https://doi.org/10.1017/S0022112003006347 Published online by Cambridge University Press

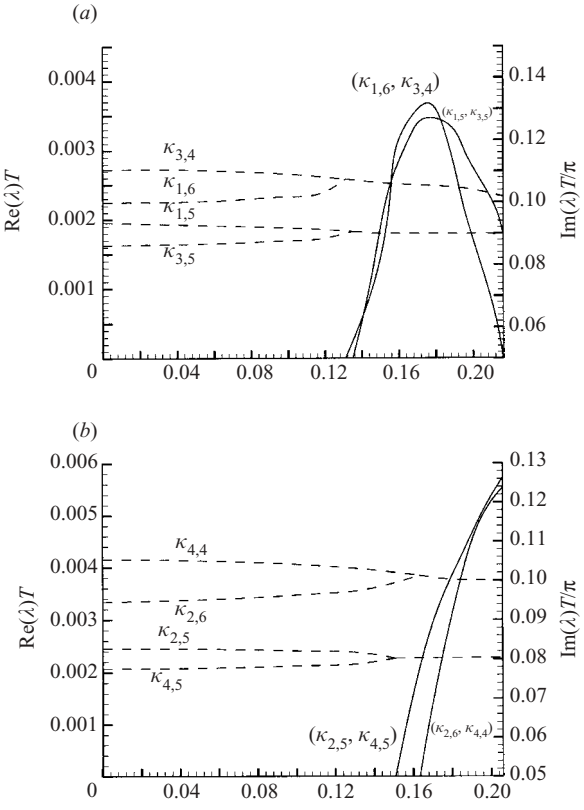


FIGURE 14. —, growth rate Re(λ) and – – –, eigen-frequency Im(λ) of three-dimensional perturbations (labelled by their dominant components) for non-axisymmetric base standing waves with (*a*) wavenumber $k_{2,5}$ and (*b*) $k_{3,5}$ in a circular tank as a function of the fundamental wave steepness ε.

5. Mechanism of the standing-wave instability

For propagating (Stokes) waves, it is known that the class I and class II instabilities are results of (third-order) quartet and (fourth-order) quintet resonant interactions between the fundamental wave and the unstable perturbations (Philips 1960; McLean 1982). Such resonances have been shown, for example, in the dynamics of beams and plates (e.g. Nayfeh & Mook 1979; Kyoyul & Nayfeh 1996). In this section, we show that the standing-wave instabilities in §§4.1 and 4.2 are also results of high-order (quartet and quintet) resonances between the fundamental standing wave and its unstable modes. The resonance condition here is, however, more similar to the nonlinear resonant interactions or bifurcations that occur in a parametrically resonated basin (see e.g. Bridges 1987); and different from that for propagating waves in that only a frequency relationship, but no wavenumber condition, is involved.

5.1. *Plane base standing waves*

Let ω_p, Ω_p be the linear and nonlinear frequencies, respectively, of a plane standing wave of wavenumber p. Figure 16 plots Ω_8 (obtained numerically) as a function of kA, compared to select combinations of linear frequencies ω_p. As kA increases, Ω_8 intersects successively $(\omega_7+\omega_9)/2$, $(\omega_{14}+\omega_{22})/3$ and $(\omega_6+\omega_{10})/2$. The conditions for internal resonances obtain at these frequency crossing points: quartet resonances for

https://doi.org/10.1017/S0022112003006347 Published online by Cambridge University Press

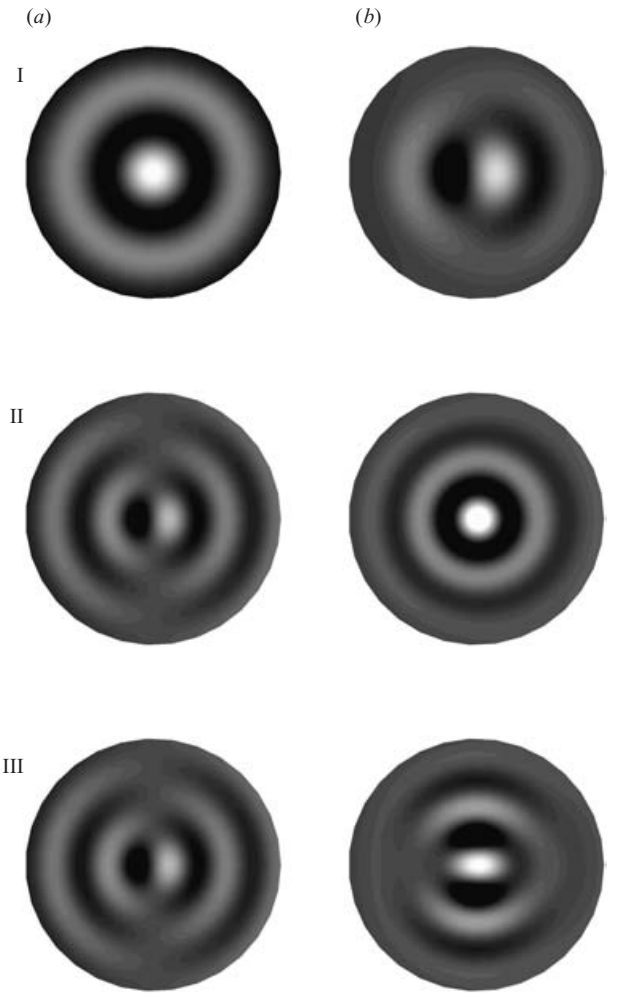


FIGURE 15. (*a*) Instantaneous free-surface elevation of the base standing waves, and (*b*) the corresponding result, after significant development of the (dominant) unstable perturbations. The base flow (k) and perturbation (κ) wavenumbers for the sample cases are respectively: I, $k_{0,4}$ and $\kappa_{1,3}, \kappa_{1,4}$; II, $k_{1,5}$ and $\kappa_{0,5}, \kappa_{0,6}$; III $k_{1,5}$ and $\kappa_{2,4}, \kappa_{2,5}$.

Ω_8 (counted twice), and the mode pairs ω_7 and ω_9, and ω_6 and ω_{10}, respectively; and quintet resonance for Ω_8 (counted thrice) and the mode pair ω_{14} and ω_{22}. These correspond directly to the results of figure 4. Since quintet resonance is one order higher in wave steepness than quartet resonance, we expect that the former would have a smaller growth rate. This is also consistent with the numerical findings (figure 4*b*).

For three-dimensional instability, similar internal resonances obtain. The instability we find in §4.1.2 (under the condition $\Omega_p \simeq \omega_p$) corresponds simply to quartet resonances satisfying the conditions: $\Omega_p \simeq 2\omega_p - \omega_p$, $2\Omega_p - \omega_p \simeq \omega_p$ and $2\Omega_p - \Omega_p \simeq \omega_p$.

5.2. *Standing waves in a circular tank*

Let $\omega_{\ell,\nu}$, $\Omega_{\ell,\nu}$ be the linear and nonlinear frequencies, respectively, of a standing wave in a circular tank with wavenumber $k_{\ell,\nu}$. For moderate to deep tank depth, $\omega_{\ell,\nu}$

https://doi.org/10.1017/S0022112003006347 Published online by Cambridge University Press

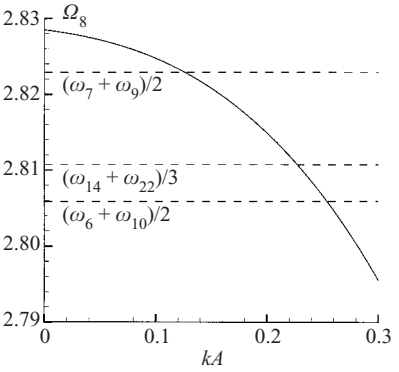


FIGURE 16. Nonlinear frequency Ω_8 of the plane standing wave k_8 as a function of the wave steepness kA, plotted with the linear frequency combinations $(\omega_7+\omega_9)/2$, $(\omega_6+\omega_{10})/2$ and $(\omega_{14}+\omega_{22})/3$. The plotted frequencies are normalized by ω_1.

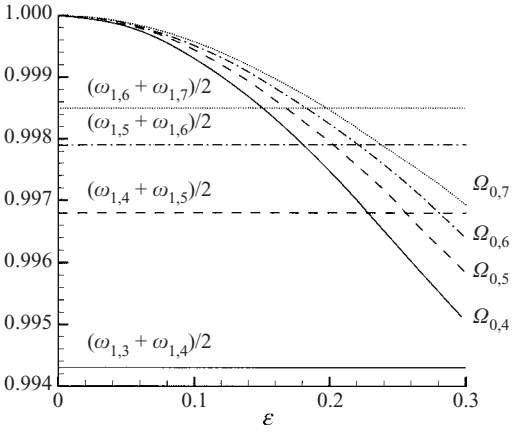


FIGURE 17. Nonlinear frequency $\Omega_{0,\nu}$ of an axisymmetric standing wave in a circular tank ($h/R=0.5$) of wavenumber $k_{0,\nu}$ as a function of wave steepness ε, plotted against the linear frequency combination $(\omega_{1,\nu-1}+\omega_{1,\nu})/2$. For each ν, —, $\nu=4$, – – –, 5, —·—, 6, and ···, 7, the values are normalized by $\omega_{0,\nu}$ (curves corresponding to different ν actually do not cross).

are shown to satisfy the approximate relationships (using the asymptotic property of Bessel functions of large orders, e.g. Abramowitz & Stegun 1972):

$$2\omega_{0,\nu} \simeq \omega_{1,\nu}+\omega_{1,\nu-1}, \tag{5.1}$$

$$2\omega_{\ell,\nu} \simeq \omega_{\ell-1,\nu}+\omega_{\ell-1,\nu+1}, \tag{5.2}$$

$$2\omega_{\ell,\nu} \simeq \omega_{\ell+1,\nu-1}+\omega_{\ell-1,\nu}, \tag{5.3}$$

$$2\omega_{\ell,\nu} \simeq \omega_{\ell-1,\nu+1}+\omega_{\ell+1,\nu-1}, \tag{5.4}$$

$$2\omega_{\ell,\nu} \simeq \omega_{\ell-1,\nu}+\omega_{\ell+1,\nu}, \tag{5.5}$$

for $\ell, \nu = 1, 2, \ldots$. For limited steepness of the base standing wave, $\Omega_{\ell,\nu}$ and $\omega_{\ell,\nu}$ differ only slightly (e.g. figure 3). Thus, we can use the above equations to deduce the combination of wave modes among which quartet resonance might occur.

Figure 17 plots $\Omega_{0,\nu}$ (obtained numerically) for $\nu=4, 5, 6, 7$ as a function of ε. For $\nu=7, 6, 5$, these $\Omega_{0,\nu}$ curves cross the linear-frequency combinations $(\omega_{1,\nu-1}+\omega_{1,\nu})/2$ (see (5.1)) at $\varepsilon \cong 0.20, 0.22, 0.26$, respectively. Thus, the conditions for internal quartet resonances, and hence instability, obtain at these points for the associated

https://doi.org/10.1017/S0022112003006347 Published online by Cambridge University Press

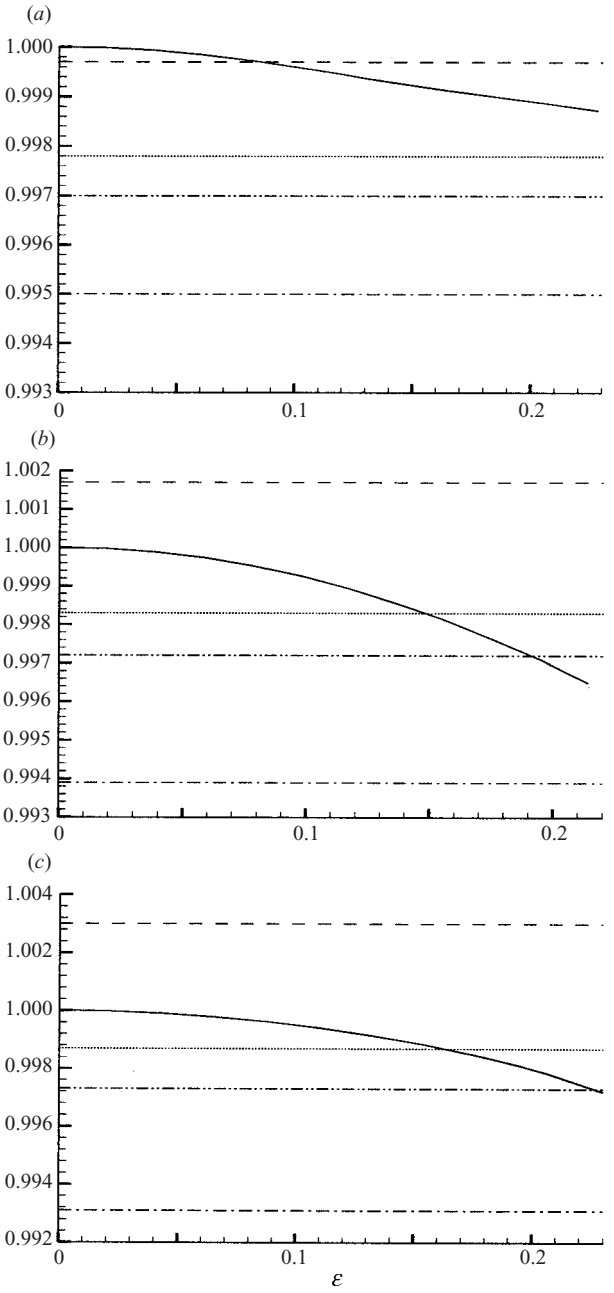


FIGURE 18. —, nonlinear frequency $\Omega_{\ell,5}$ of a non-axisymmetric standing wave in a circular tank ($h/R = 0.5$) of wavenumber $k_{\ell,5}$ with (*a*) $\ell = 1$, (*b*) 2 and (*c*) 3 as a function of wave steepness ε. Also plotted are the linear frequency combinations – – –, $(\omega_{\ell-1,5} + \omega_{\ell-1,6})/2$; · · ·, $(\omega_{\ell-1,5} + \omega_{\ell+1,5})/2$; — · —, $(\omega_{\ell-1,6} + \omega_{\ell+1,4})/2$; — · —, $(\omega_{\ell+1,4} + \omega_{\ell+1,5})/2$. All frequencies are normalized by $\omega_{\ell,5}$.

perturbations containing the dominant components $\kappa_{1,\nu-1}$ and $\kappa_{1,\nu}$. This is precisely the finding in § 4.2.1.

Similar frequency-crossings exist for non-axisymmetric standing waves $k_{\ell,\nu}$ ($\ell \geqslant 1$). In figure 18, we plot the nonlinear frequencies $\Omega_{\ell,5}$, $\ell = 1, 2, 3$ as functions of ε

https://doi.org/10.1017/S0022112003006347 Published online by Cambridge University Press

together with the four linear-frequency combinations specified by the right-hand sides of (5.2)–(5.5). As ε increases, frequency crossings between Ω and combinations of ω occur corresponding to internal (quartet) resonance instabilities. In the range of ε considered, $\Omega_{1,5}$ crosses $(\omega_{0,5}+\omega_{0,6})/2$ (only), while $\Omega_{\ell,5}$, $\ell = 2, 3$, cross both $(\omega_{\ell-1,6}+\omega_{\ell+1,4})/2$ and $(\omega_{\ell-1,5}+\omega_{\ell+1,5})/2$. These linear frequency combinations correspond directly to the dominant components of the unstable perturbations we found in § 4.2.2.

By considering the (nonlinear) frequencies of standing waves and the way they combine, this simple analysis shows that the instabilities of standing waves we found in § 4 are a direct consequence of high-order internal resonances. The frequency conditions for such resonances identify the dominant component(s) of the corresponding unstable modes. The base standing-wave amplitudes/steepnesses at which such conditions obtain provide a crude estimate for the threshold values above which such instabilities occur.

Finally, we comment on an interesting consequence of the instability we find to the transition from axisymmetry to non-axisymmetry of standing waves in a circular tank. From § 4.2, we see that an axisymmetric standing wave $k_{0,\nu}$ is unstable to perturbations containing wavenumber components $\kappa_{1,\nu-1}$ and $\kappa_{1,\nu}$. As modes with these components grow in amplitude beyond a threshold value, they themselves become unstable to $\ell = 2$ perturbations. This process is repeated resulting in increasingly large ℓ modes: from $\kappa_{\ell,\nu}$ to $\kappa_{\ell+1,\nu-1}$ and $\kappa_{\ell+1,\nu}$ (as well as to $\kappa_{\ell-1,\nu+1}, \kappa_{\ell+1,\nu-1}$)). With sufficient amplitude (and time), this mechanism of energy cascade to increasing azimuthal (and radial) mode numbers could result in highly three-dimensional wave patterns. This offers a possible explanation for the experimental observation of Gollub & Meyer (1983) in which the surface waves in a vertically oscillated circular tank change from axisymmetric to non-axisymmetric as the oscillation amplitude exceeds a critical value.

6. Conclusions

The three-dimensional instability of nonlinear two- and three-dimensional standing surface waves is investigated numerically based on the transition matrix method. An efficient high-order spectral element (HOSE) method is developed and applied to this analysis.

Two classes of base standing waves are considered: (i) plane standing waves in deep water; and (ii) three-dimensional standing waves in a circular basin. For the former, both two- and three-dimensional instabilities are found. For two-dimensional instability, we obtain quantitative comparisons with the fully nonlinear results of Mercer & Roberts (1992) for the frequency and growth rate of the unstable modes. When three-dimensional perturbations are considered, we find that a plane standing wave is unstable to modes, at arbitrary oblique angles, satisfying a frequency condition.

For standing waves in a circular tank, we find that there is a threshold wave amplitude beyond which the base wave (of any azimuthal and radial mode numbers) is unstable to (three-dimensional) perturbations. The mode numbers for the unstable modes are identified and are shown to satisfy a simple relation to those of the base wave.

We further show that the instabilities we find are direct consequences of quartet internal resonances, and offer a possible explanation for the transition of standing waves in circular tanks from axisymmetry to non-axisymmetry observed in experiments.

https://doi.org/10.1017/S0022112003006347 Published online by Cambridge University Press

Finally, it should be noted that the present HOSE approach is limited by convergence to moderate wave steepness. In many cases, initial instabilities may lead to steep, even breaking, waves. The dynamics of these very steep standing waves (e.g. Jian, Perlin & Schultz 1998; Longuet-Higgins & Dommermuth 2001; Longuet-Higgins & Drazen 2002) is beyond the validity of HOSE and the scope of this study.

This research is supported financially by grants from the office of Naval Research whose sponsorship is gratefully acknowledged.

Appendix A. Formulation and implementation of the high-order spectral-element method

For completeness, we present here an outline of the formulation and implementation of the high-order spectral element (HOSE) method for the computation of nonlinear wave dynamics. The details are found in Zhu (2000).

A.1. *High-order expansions*

In HOSE, as in HOS, we expand Φ in a perturbation series with respect to the small wave steepness parameter ε up to order M:

$$\Phi(\boldsymbol{r}, t) = \sum_{m=1}^{M} \Phi^{(m)}(\boldsymbol{r}, t), \tag{A 1}$$

where $\boldsymbol{r} = (x, y, z)$, $()^{(m)}$ denotes a quantity of the order $O(\varepsilon^m)$. Expanding the free-surface potential Φ^s in Taylor series about the mean free surface $\bar{S}_F$ (i.e. $z = 0$) and collecting terms in each order $O(\varepsilon^m)$, we obtain a sequence of Dirichlet boundary conditions for $\Phi^{(m)}$ on $\bar{S}_F$:

$$\Phi^{(m)} = f^{(m)} \qquad \text{on } \bar{S}_F, \tag{A 2}$$

where $f^{(1)}(\boldsymbol{x}, t) = \Phi^s$ and

$$f^{(m)}(\boldsymbol{x}, t) = -\sum_{\ell=1}^{m-1} \frac{\zeta^\ell}{\ell!} \frac{\partial^\ell}{\partial z^\ell} \Phi^{(m-\ell)}(\boldsymbol{x}, 0, t), \quad m = 2, 3, \ldots, M.$$

On the fixed body surface $\bar{S}_B$ (for body with small motions, a high-order treatment similar to that for the free-surface should be employed, see Zhu *et al.* 1999), we have a sequence of Neumann boundary conditions for $\Phi^{(m)}$, $m = 1, \ldots, M$:

$$\Phi_n^{(m)} = 0 \qquad \text{on } \bar{S}_B. \tag{A 3}$$

With these expansions, the original nonlinear boundary-value problem for Φ is decomposed into a sequence of linear boundary-value problems for $\Phi^{(m)}$, $m = 1, \ldots, M$, consisting of the Laplace equation ($\nabla^2 \Phi^{(m)} = 0$) inside the mean fluid domain, Dirichlet boundary condition (A 2) on $\bar{S}_F$, and Neumann boundary condition (A 3) on $\bar{S}_B$.

The sequence of linear problems for $\Phi^{(m)}$, $m = 1, 2, \ldots, M$ are now solved in order starting from $m = 1$. The immediate interest is the surface vertical velocity Φ_z^s:

$$\Phi_z^s \equiv \Phi_z(\boldsymbol{x}, \zeta, t) = \sum_{m=1}^{M} \sum_{\ell=0}^{M-m} \frac{\zeta^\ell}{\ell!} \frac{\partial^{\ell+1}}{\partial z^{\ell+1}} \Phi^{(m)}(\boldsymbol{x}, 0, t). \tag{A 4}$$

https://doi.org/10.1017/S0022112003006347 Published online by Cambridge University Press

Substituting Φ_z^s into (2.2), the free-surface elevation ζ and potential Φ^s are updated by explicit time integration (in this work we use a fourth-order Runge–Kutta scheme).

A.2. *Spectral-element approach for the boundary-value solution*

To solve the boundary-value problem for $\Phi^{(m)}$, $m = 1, 2, \ldots, M$, we divide the boundary $\bar{S}_F$ and $\bar{S}_B$, respectively, into N_{FE} and N_{BE} piecewise smooth elements. On each element, we expand the potential $\Phi^{(m)}$ and normal velocity $\Phi_n^{(m)}$ in spectral series:

$$\Phi^{(m)}(\boldsymbol{r}, t) = \sum_{\ell=1}^{\infty} \alpha_{j\ell}^F(t)\Psi_{j\ell}^F(\boldsymbol{r}), \qquad \Phi_n^{(m)}(\boldsymbol{r}, t) = \sum_{\ell=1}^{\infty} \beta_{j\ell}^F(t)\Theta_{j\ell}^F(\boldsymbol{r}), \tag{A 5}$$

for $\boldsymbol{r} \in \bar{S}_{F_j}$, $j = 1, \ldots, N_{FE}$ and

$$\Phi^{(m)}(\boldsymbol{r}, t) = \sum_{\ell=1}^{\infty} \alpha_{j\ell}^B(t)\Psi_{j\ell}^B(\boldsymbol{r}), \qquad \Phi_n^{(m)}(\boldsymbol{r}, t) = \sum_{\ell=1}^{\infty} \beta_{j\ell}^B(t)\Theta_{j\ell}^B(\boldsymbol{r}), \tag{A 6}$$

for $\boldsymbol{r} \in \bar{S}_{B_j}$, $j = 1, \ldots, N_{BE}$. In the above, $\Psi_{j\ell}^F$ ($\Theta_{j\ell}^F$) and $\Psi_{j\ell}^B$ ($\Theta_{j\ell}^B$) are the ℓth spectral basis functions for $\Phi^{(m)}$ ($\Phi_n^{(m)}$) on the jth free-surface and body elements, respectively; $\alpha_{j\ell}^F$ ($\beta_{j\ell}^F$) and $\alpha_{j\ell}^B$ ($\beta_{j\ell}^B$) are the corresponding modal amplitudes.

We now apply Green's theorem to $\Phi^{(m)}$ and the appropriate free-space (Rankine) Green function, and upon truncating the expansions (A 5) and (A 6) to finite numbers of free-surface (N_{FM}) and body (N_{BM}) spectral modes (per element), we obtain the following linear system of equations:

$$\sum_{j=1}^{N_{BE}} \sum_{\ell=1}^{N_{BM}} \alpha_{j\ell}^B(t) C_{j\ell}^{BF}(\boldsymbol{r}) - \sum_{j=1}^{N_{FE}} \sum_{\ell=1}^{N_{FM}} \beta_{j\ell}^F(t) D_{j\ell}^{FF}(\boldsymbol{r}) = R_F(\boldsymbol{r}, t), \qquad \boldsymbol{r} \in \bar{S}_{F_j} \tag{A 7}$$

and

$$\sum_{j=1}^{N_{BE}} \sum_{\ell=1}^{N_{BM}} \alpha_{j\ell}^B(t) C_{j\ell}^{BB}(\boldsymbol{r}) - \sum_{j=1}^{N_{FE}} \sum_{\ell=1}^{N_{FM}} \beta_{j\ell}^F(t) D_{j\ell}^{FB}(\boldsymbol{r}) = R_B(\boldsymbol{r}, t), \qquad \boldsymbol{r} \in \bar{S}_{B_j}. \tag{A 8}$$

The forcing terms R_F and R_B are known:

$$R_F(\boldsymbol{r}, t) = -\sum_{j=1}^{N_{FE}} \sum_{\ell=1}^{N_{FM}} \alpha_{j\ell}^F(t) C_{j\ell}^{FF}(\boldsymbol{r}) + \sum_{j=1}^{N_{BE}} \sum_{\ell=1}^{N_{BM}} \beta_{j\ell}^B(t) D_{j\ell}^{BF}(\boldsymbol{r}) \tag{A 9}$$

and

$$R_B(\boldsymbol{r}, t) = -\sum_{j=1}^{N_{FE}} \sum_{\ell=1}^{N_{FM}} \alpha_{j\ell}^F(t) C_{j\ell}^{FB}(\boldsymbol{r}) + \sum_{j=1}^{N_{BE}} \sum_{\ell=1}^{N_{BM}} \beta_{j\ell}^B(t) D_{j\ell}^{BB}(\boldsymbol{r}). \tag{A 10}$$

In the above, the influence coefficients are known and given by integrals over the boundary elements in terms of the free-surface and body basis functions and the Green function. From (A 7) and (A 8), the unknown modal amplitudes $\alpha_{j\ell}^B$ and $\beta_{j\ell}^F$ are solved.

A.3. *Choice of spectral basis functions*

Unlike in HOS, the HOSE local basis functions (Ψ and Θ) in (A 5) and (A 6) are not required to satisfy specific essential boundary conditions. While there is significant flexibility in the choice of these functions, a desirable requirement is the exponential

https://doi.org/10.1017/S0022112003006347 Published online by Cambridge University Press

convergence of the expansions for the element. Thus, for example, Fourier expansions are used when boundary conditions are periodic, but are inappropriate when non-periodic boundary conditions apply.

For the two-dimensional plane standing wave in a rectangular basin, the lateral boundary conditions are rendered periodic, and a single (global or super) free-surface element with Fourier global basis functions (i.e. HOS) are used.

For standing waves in a circular tank with vertical sidewall and a horizontal bottom (say of radius R and depth h), we divide $\bar{S}_F$ into N_{FE} concentric (circular) annular elements S_{F_j}, $j = 1, \ldots, N_{FE}$, with $(j-1)\Delta R \leqslant r \leqslant j\Delta R$, $\Delta R \equiv R/N_{FE}$ (and $0 \leqslant \theta \leqslant 2\pi$). The sidewall ($r = R$, $-h \leqslant z \leqslant 0$) and bottom ($z = -h$, $0 \leqslant r \leqslant R$) of the tank are each treated as a single element, tagged as $\bar{S}_w$ and $\bar{S}_b$, respectively (i.e. $\bar{S}_B = \bar{S}_w + \bar{S}_b$). For these spectral elements, an appropriate choice for the basis functions for both the free-surface and wall/bottom elements is Fourier–Chebyshev in the azimuthal–radial directions. For S_{F_j}, $j = 1, \ldots, N_{FE}$, we employ a double expansion with $N_{F\theta}$ and N_{Fr} Fourier and Chebyshev modes:

$$\Psi^F_{jpq}(\boldsymbol{r}) \equiv \Psi^F_{pq} = T_q(r)\mathrm{e}^{\mathrm{i}p\theta}, \quad |p| = 0, 1, \ldots, N_{F\theta}/2; \;\; q = 0, 1, \ldots, N_{Fr}; \tag{A 11}$$

where T_q represents the qth-order Chebyshev polynomial of the first kind. For $\bar{S}_w$ and $\bar{S}_b$, we use, respectively, the basis functions:

$$\Psi^w_{pq}(\boldsymbol{r}) = T_q(z)\mathrm{e}^{\mathrm{i}p\theta}, \quad |p| = 0, 1, \ldots, N_{w\theta}/2; \;\; q = 0, 1, \ldots, N_{wz}; \tag{A 12}$$

$$\Psi^b_{pq}(\boldsymbol{r}) = T_q(r)\mathrm{e}^{\mathrm{i}p\theta} \quad |p| = 0, 1, \ldots, N_{b\theta}/2; \;\; q = 0, 1, \ldots, N_{br}. \tag{A 13}$$

The same sets of basis functions are used for Θ^F and Θ^B, $B = w, b$.

Note that, for this geometry, in theory, $N_{FE} = 1$ suffices. In practice, for given machine accuracy, the maximum number of Chebyshev modes, say N_C, we can use in an element is limited by the condition number of the resulting equation system. Thus, as a practical matter, we place an upper limit on N_C (typically $N_C < \sim 32$ for double precision) and increase the number of elements, generally N_{FE}, to achieve the necessary accuracy/convergence. For this problem and value of N_C, a single element for $\bar{S}_b$ and $\bar{S}_w$, respectively, is found to be sufficient.

A.4. *Evaluation of high z-derivatives of* $\Phi^{(m)}$

To evaluate the Dirichlet boundary condition for $\Phi^{(m)}$ (cf. (A 2)) and the free-surface vertical velocity (cf. (A 4)), we need to determine, to high orders, the z-derivatives of $\Phi^{(m)}$, i.e. $\Phi^{(m)}_{zz}, \Phi^{(m)}_{zzz}, \ldots$ on the mean free surface $\bar{S}_F$. To do that, we employ an approach wherein the high-order z-derivatives of $\Phi^{(m)}$ are solved directly via the associated boundary-value problems. For example, to evaluate $\Phi^{(m)}_{zz}$, the boundary-value problem is the same as that for $\Phi^{(m)}$, but with $\Phi^{(m)}$ replaced by $\Phi^{(m)}_z$. The additional computational effort is not significant since the equation system for the boundary-value problem is the same and needs to be inverted only once (for a given mean geometry, independent of order or time). Note that to obtain high accuracy in the evaluation, it is important to ensure the requisite continuity across inter-element boundaries, at least C^1, for example, for $\Phi^{(m)}_z$ on $\bar{S}_F$. To do that, we replace the Dirichlet boundary condition at the edges of boundary elements by the continuity condition. Details are presented in Zhu (2000).

A.5. *Numerical implementation*

In a pseudospectral approach, we employ a collocation method to solve equations (A 7) and (A 8) for the unknown modal amplitudes $\alpha^B_{j\ell}$ and $\beta^F_{j\ell}$. To ensure

https://doi.org/10.1017/S0022112003006347 Published online by Cambridge University Press

exponential convergence, the collocation points are distributed uniformly for the Fourier expansion and placed at the local maxima of $T_{N_C}(r)$ for the Chebyshev spectral representation containing N_C terms. The resulting system contains $N_F + N_B$ equations ($N_F = N_{FM}N_{FE}$, $N_B = N_{BM}N_{BE}$) which are written formally as:

$$\begin{bmatrix} C^{BF} & D^{FF} \\ C^{BB} & D^{FB} \end{bmatrix} \begin{Bmatrix} \alpha^B \\ \beta^F \end{Bmatrix} = \begin{Bmatrix} R^F \\ R^B \end{Bmatrix} \tag{A 14}$$

Here, C^{BF}, D^{FF}, C^{BB} and D^{FB} are, respectively, the $N_B \times N_F$, $N_F \times N_F$, $N_B \times N_B$ and $N_F \times N_B$ modal influence matrices given in terms of the basis functions; R^F and R^B are vectors given, respectively, by R_F and R_B, and α^B and β^F are the vectors of unknown modal amplitudes.

The matrix inversion in (A 14) is required only once for a given problem geometry, and is independent of the time, order or base flow. In practice, the computational effort of HOSE is dominated by the operation account at each time step. For the general wave–body interaction problem, an operation of $O((N_F + N_B)^2)$ is required. For the problem of standing-wave motion in a circular basin, the computational effort is reduced by a factor $N_{F\theta}$ by using fast Fourier transforms in the azimuthal direction, where $N_{F\theta}$ is the total number of Fourier modes. The total operation count for the simulation of finite-amplitude waves in a circular tank including wave–wave and wave–wall interactions up to order M is $O(M(N_F + N_B)^2/N_{F\theta})$ per time step.

Appendix B. Determination of the base flow for a nonlinear standing wave

To determine the frequency and configuration of a nonlinear standing wave (satisfying (2.4), we seek an initial free-surface profile $\zeta(\boldsymbol{x}, t=0)$ for an initial free-surface velocity potential $\Phi^s(\boldsymbol{x}, t = 0) = 0$ such that Φ^s, through the nonlinear evolution, returns to zero again after some time (corresponding to $T/2$). To do this, we follow the Newtonian iteration method of MR, but use HOSE computations for the nonlinear wave simulation.

The procedure to obtain a standing wave of a specified amplitude A is as follows: (i) given an initial (estimate of) $\zeta(\boldsymbol{x}, 0)$ and T (and $\Phi^s(\boldsymbol{x}, 0) = 0$), use HOSE to obtain $\zeta(\boldsymbol{x}, T/2)$ and $\Phi^s(\boldsymbol{x}, T/2)$; (ii) compute the error vector $\mathscr{E} = \{E_j\}$:

$$E_j = \begin{cases} \Phi^s(\boldsymbol{x}_j, T/2), & j = 1, \ldots, N_F, \\ \zeta(\boldsymbol{x}, 0)_{\max} - \zeta(\boldsymbol{x}, T/2)_{\min} - 2A, & j = N_F + 1, \end{cases} \tag{B 1}$$

where $\boldsymbol{x}_j$, $j = 1, \ldots, N_F$ are the HOSE collocation points on $\bar{S}_F$; (iii) compute the Jacobian matrix $\mathscr{J} = [J_{j\ell}]$:

$$J_{j\ell} = \begin{cases} \partial E_j/\partial \zeta(\boldsymbol{x}_\ell, 0), & \ell = 1, \ldots, N_F, \\ \partial E_j/\partial T, & \ell = N_F + 1, \end{cases} \tag{B 2}$$

for $j = 1, \ldots, N_F + 1$; (iv) update $\zeta(\boldsymbol{x}, t = 0)$ and T using $\mathscr{J}$. The Newtonian iteration process (i)–(iv) is repeated until $||\mathscr{E}||$ becomes smaller than a preset tolerance (set to be 10^{-12} in the present study).

Generally, we use the linearized $\zeta(\boldsymbol{x}, 0)$ and T as initial guess. To accelerate the convergence for steeper waves, a useful alternative is to obtain the initial guess using (Richardson) extrapolation of the (converged) nonlinear solutions for smaller amplitudes.

https://doi.org/10.1017/S0022112003006347 Published online by Cambridge University Press

REFERENCES

Abramowitz, M. & Stegun, I. A. 1972 *Handbook of Mathematical Functions*. Dover.

Becker, J. M. & Miles, J. W. 1992 Progressive radial cross-waves. *J. Fluid Mech.* **245**, 29–46.

Bender, C. M. & Orszag, S. A. 1978 *Advanced Mathematical Methods for Scientists and Engineers*. McGraw-Hill.

Benjamin, T. B. & Feir, J. E. 1967 The disintegration of wave trains on deep water. 1. Theory. *J. Fluid Mech.* **27**, 417–430.

Bridges, T. J. 1987 Secondary bifurcation and change of type for three-dimensional standing waves in finite depth. *J. Fluid Mech.* **179**, 137–153.

Canuto, C., Hussaini, M. Y., Quarteroni, A. & Zang, T. A. 1988 *Spectral Methods in Fluid Dynamics*. Springer.

Coddington, D. A. & Levinson, N. 1955 *Theory of Ordinary Differential Equations*. McGraw-Hill.

Dommermuth, D. G. & Yue, D. K. P. 1987 A high-order spectral method for the study of nonlinear gravity waves. *J. Fluid Mech.* **184**, 267–288.

Gollub, J. P. & Meyer, W. 1983 Symmetry-breaking instabilities on a fluid surface. *Physica* **6D**, 337–346.

Ioualalen, M. & Kharif, C. 1994 On the subharmonic instabilities of steady three-dimensional deep water waves. *J. Fluid Mech.* **262**, 265–291.

Ioualalen, M., Roberts, A. J. & Kharif, C. 1996 On the observability of finite-depth short-crested water waves. *J. Fluid Mech.* **322**, 1–19.

Jian, L., Perlin, M. & Schultz, W. W. 1998 Period tripling and energy dissipation of breaking standing waves. *J. Fluid Mech.* **369**, 273–299.

von Kerczek, C. & Davis, S. H. 1975 Calculation of transition matrices. *AIAA J.* **13**, 1400–1403.

Kimmoun, O., Ioualalen, M. & Kharif, C. 1999 Instabilities of steep short-crested surface waves in deep water. *Phys. Fluids* **11**, 1679–1681.

Kyoyul, O. H. & Nayfeh, A. H. 1996 Nonlinear combination resonances in cantilever composite plates. *Nonlinear Dyn.* **11**, 143–169.

Liu, Y., Dommermuth, D. G. & Yue, D. K. P. 1992 A high-order spectral method for nonlinear wave–body interactions. *J. Fluid Mech.* **245**, 115–136.

Liu, Y. & Yue, D. K. P. 1998 On generalized Bragg scattering of surface waves by bottom ripples. *J. Fluid Mech.* **356**, 297–326.

Longuet-Higgins, M. S. 1978*a* The instabilities of gravity waves of finite amplitude in deep water I. Superharmonics. *Proc. R. Soc. Lond.* A **360**, 471–488.

Longuet-Higgins, M. S. 1978*b* The instabilities of gravity waves of finite amplitude in deep water I. Subharmonics. *Proc. R. Soc. Lond.* A **360**, 489–505.

Longuet-Higgins, M. S. & Dommermuth, D. G. 2001 On the breaking of standing waves by falling jets. *Phys. Fluids* **13**, 1652–1659.

Longuet-Higgins, M. S. & Drazen, D. A. 2002 On steep gravity waves meeting a vertical wall: a triple instability. *J. Fluid Mech.* **466**, 305–318.

Mack, L. R. 1962 Periodic, finite-amplitude, axisymmetric gravity waves. *J. Geophys. Res.* 67, no. 2.

McLean, J. W. 1982 Instabilities of finite-amplitude water waves. *J. Fluid Mech.* **114**, 315–330.

Martin, T. 1932 *Faraday's Diary*, vol. 1, July 5th, 1831 entry. G. Bell.

Mei, C. C. 1983 *The Applied Dynamics of Ocean Surface Waves*. John Wiley.

Mercer, G. N. & Roberts, A. J. 1992 Standing waves in deep water: their stability and extreme form. *Phys. Fluids* A **4**, 259–269.

Miles, J. W. 1984*a* Resonantly forced surface waves in a circular cylinder. *J. Fluid Mech.* **149**, 15–31.

Miles, J. W. 1984*b* Nonlinear Faraday Resonance. *J. Fluid Mech.* **146**, 285–302.

Miles, J. W. 1984*c* Internally resonant surface waves in a circular cylinder. *J. Fluid Mech.* **149**, 1–14.

Nayfeh, A. H. & Mook, D. T. 1979 *Nonlinear Oscillations*. John Willey.

Philips, O. M. 1960 On the dynamics of unsteady gravity waves of finite amplitude. Part 1. The elementary interactions. *J. Fluid Mech.* **9**, 193–217.

Pierce, R. D. & Knobloch, E. 1994 On the modulational stability of traveling and standing water waves. *Phys. Fluids* **6**, 1177–1190.

Su, M. Y. 1982 Three-dimensional deep-water waves. Part I. Experimental measurement of skew and symmetric wave patterns. *J. Fluid Mech.* **124**, 73–108.

https://doi.org/10.1017/S0022112003006347 Published online by Cambridge University Press

Tatsuno, M., Inoue, S. & Okabe, J. 1969 Transfiguration of surface waves. *Rep. Res. Inst. Appl. Mech. Kyushu University* **17**, 195–215.

Tsai, W. T. & Yue, D. K. P. 1987 Numerical calculation of nonlinear axisymmetric standing waves in a circular basin. *Phys. Fluids* **30**, 3441–3447.

Vanden-Broeck, J. M. & Schwartz, L. W. 1981 *Phys. Fluids* **24**, 812.

Xue, M., Xu, H., Liu, Y. & Yue, D. K. P. 2001 Computations of fully-nonlinear three-dimensional wave–wave and wave–body interactions. Part 1. Dynamics of three-dimensional steep waves. *J. Fluid Mech.* **438**, 11–39.

Yuen, H. C. & Ferguson, W. E. jr 1978 Relationship between Benjamin–Feir instability and recurrence in the nonlinear Schrödinger equation. *Phys. Fluids* **21**, 1275–1278.

Yuen, H. C. & Lake, B. M. 1980 Instabilities of waves on deep water. *Annu. Rev. Fluid Mech.* **12**, 303–334.

Zakharov, V. E. 1968 Stability of periodic waves of finite amplitude on the surface of a deep fluid. *J. Appl. Mech. Tech. Phys.* **9**, 190–194 (English Trans.).

Zhang, J., Hong, K. & Yue, D. K. P. 1993 Effects of wavelength ratio on wave-mode modelling. *J. Fluid Mech.* **248**, 107–127.

Zhu, Q. 2000 Features of nonlinear wave–wave and wave–body interactions. PhD thesis, Massachusetts Institute of Technology.

Zhu, Q., Tjavaras, A. A., Liu Y., Yue, D. K. P. & Triantafyllou, M. S. 1999 Mechanics of nonlinear short-wave generation by a moored near-surface buoy. *J. Fluid Mech.* **381**, 305–335.

https://doi.org/10.1017/S0022112003006347 Published online by Cambridge University Press